

**Temperatures recorded by cosmogenic noble gases since the last glacial
maximum in the Maritime Alps**

Marissa M. Tremblay^{1,2,*}, David L. Shuster^{1,2}, Matteo Spagnolo³, Hans Renssen⁴, Adriano
Ribolini⁵

¹Department of Earth and Planetary Science, University of California, Berkeley, Berkeley, CA,
94720-4767 USA

²Berkeley Geochronology Center, Berkeley, CA, 94709, USA

³Department of Geography and Environment, School of Geosciences, University of Aberdeen,
Aberdeen, AB24 3UF, UK

⁴Department of Natural Sciences and Environmental Health, University College of Southeast
Norway, 3800 Bø, Norway

⁵Dipartimento di Scienze della Terra, Università di Pisa, 56126 Italy.

*Now located at Scottish Universities Environmental Research Centre, Rankine Avenue, East
Kilbride, G75 0QF, UK

Correspondence to: Marissa M. Tremblay (marissa.tremblay@glasgow.ac.uk)

ABSTRACT

While proxy records have been used to reconstruct late Quaternary climate parameters throughout the European Alps, our knowledge of deglacial climate conditions in the Maritime Alps is limited. Here, we report temperatures recorded by a new and independent geochemical technique—cosmogenic noble gas paleothermometry—in the Maritime Alps since the last glacial maximum (LGM). We measured cosmogenic ^3He in quartz from boulders in nested moraines in the Gesso Valley, Italy. Paired with cosmogenic ^{10}Be measurements and ^3He diffusion experiments on quartz from the same boulders, the cosmogenic ^3He abundances record the temperatures these boulders experienced during their exposure. We calculate effective diffusion temperatures (EDTs) over the last ~22 ka ranging from 8 to 25°C. These EDTs, which are functionally related to, but greater than, mean ambient temperatures, are consistent with temperatures inferred from other proxies in nearby Alpine regions and those predicted by a transient general circulation model. In detail, however, we also find different EDTs for boulders from the same moraines, thus limiting our ability to interpret these temperatures. We explore possible causes for these intra-moraine discrepancies including variations in radiative heating, our treatment of complex helium diffusion, uncertainties in our grain size analyses, and unaccounted for erosion or cosmogenic inheritance.

KEYWORDS

cosmogenic isotopes; paleoclimate; Quaternary; Europe

INTRODUCTION

Data from paleoclimate proxies constrain the dynamics of Earth's climate system on timescales inaccessible with the instrumental record. Proxy observations from key intervals of Earth's past climate, such as the last glacial maximum (LGM) and subsequent deglaciation, allow us to understand how the climate system responds to a change in forcing (e.g., Schmittner et al., 2011; Annan and Hargreaves, 2013; von der Heydt et al., 2016) and evaluate the ability of climate models to simulate the climate system's response (e.g., Schmidt et al., 2014; Annan and Hargreaves, 2015; Harrison et al., 2015) both of which improve our ability to forecast future climate change (e.g., Masson-Delmotte et al., 2013). Terrestrial proxies are particularly important for assessing how changes in large scale ocean-atmosphere dynamics manifest at a regional scale in the continental settings that people inhabit and depend upon.

An extensive network of terrestrial climate reconstructions since the last glacial maximum (LGM) exists across the European Alps from pollen, chironomids (midges), organic biomarkers, and inorganic isotope systems (e.g., Bartlein et al., 2011; Blaga et al., 2013; Heiri et al., 2014; Luetscher et al., 2015). Despite such an extensive proxy network, our knowledge of deglacial climate conditions in the southern sector of the French and Italian Alps (hereafter referred to as the Maritime Alps) from proxy records is limited. Over the historical period, the Maritime Alps have been characterized by warmer mean annual temperatures (MAT), smaller annual temperature amplitudes, lower mean annual precipitation (MAP), and snow cover that is thinner and lasts for a smaller fraction of the year than in other Alpine sectors (Durand et al., 2009a, 2009b). The Maritime Alps most likely remained the warmest Alpine sector during the late Quaternary, given

that the Maritime Alps are $\sim 6^\circ$ south of the northernmost eastern Alps, and thus would have experienced greater insolation and generally higher temperatures. Warmer overall conditions are consistent with species distribution and phylogeographical models, which suggest that the Maritime Alps remained warmer than other parts of the Alps and functioned as a refugium for plant species during the last glacial period (Casazza et al., 2016). However, the handful of pollen-based reconstructions that exist from the Maritime Alps suggest that this region may have experienced distinct climatic anomalies from other Alpine regions during the Holocene. For example, during the Mid-Holocene Warm period 6,000 years ago, pollen-based reconstructions indicate that Maritime Alps winters may have been as much as 2–3 °C colder than today, while throughout the rest of the Alps winter temperatures were comparable to today (Cheddadi et al., 1996; Wu et al., 2007; Bartlein et al., 2011). For the same time period, pollen-based reconstructions indicate that the Maritime Alps were wetter, while the rest of the Alps were drier (Cheddadi et al., 1996; Bartlein et al., 2011). No pollen-based reconstructions from the Maritime Alps extend to the LGM; the nearest reconstructions are ≥ 250 km away and indicate 15–20 °C colder winter temperatures and ~ 500 mm/yr lower MAP than today (Jost et al., 2005; Bartlein et al., 2011). Similarly, there is only one reconstruction of mean July temperatures from fossil assemblages of chironomids proximal to the Maritime Alps from Lago Piccolo di Avigliana ~ 90 km away, and this record is temporally limited to 14–9.5 thousand years ago (Larocque and Finsinger, 2008). There are two proxy studies from the Maritime Alps that extend into the latest Pleistocene which we are aware of: one reporting fossil pollen assemblages in sixteen high elevation (> 1700 m) lakes (Brisset et al., 2015) and one reporting fossil chironomid assemblages from Lac Long Inférieur in France (Gandouin and Franquet, 2002). Neither of these studies interprets the proxies in terms of

quantitative climate parameters.

Due to the Maritime Alps' (1) southerly latitude, (2) generally lower elevations, and (3) proximity to the Mediterranean Sea, the late Quaternary climatic evolution and glacier dynamics in this region may have differed substantially from those in Alpine regions further north and inland (e.g., Kuhlemann et al., 2008), despite the apparent synchronicity of glacier advances during the LGM and later stadials recorded by moraines across the Alps (e.g., Ivy-Ochs et al., 2007; Kuhlemann et al., 2008; Federici et al., 2017; Monegato et al., 2017). Reconstructing temperatures in the Maritime Alps since the LGM would therefore fill a gap in an otherwise extensive network of proxy-based reconstructions of post-LGM climate across the Alps, and address the specific question of how climate evolution in the Maritime Alps during deglaciation may have differed from other Alpine sectors. For example, in combination with the positions and chronology of moraines, a well-resolved local temperature record could be used to inform a simple glacier mass balance model for valleys in the Maritime Alps during the deglacial period. With constraints on local deglacial temperatures, a mass balance model could be used to crudely invert for changes in precipitation during deglaciation (e.g., Kessler et al., 2006). This paired temperature-precipitation reconstruction could then be compared to proxy records further north and inland in the Alps to assess how climate and glacier dynamics varied across the region during deglaciation (e.g., Becker et al., 2016).

In addition to assessing climatic variability during deglaciation across the European Alps, temperature records from an independent proxy could provide tests of different methodologies for

reconstructing climate parameters over this time interval. Reconstructions of climate parameters from existing proxies in the European Alps commonly exhibit significant disagreement with climate model simulations prior to the Holocene. Pollen-based reconstructions suggest much colder temperatures, particularly in the winter, than the models predict (e.g., Jost et al., 2005), while models predict higher summertime temperatures than chironomid-based reconstructions during interstadials (Heiri et al., 2014). It is unclear whether these disagreements are attributable to limitations in the global climate models used to simulate paleoclimate, a breakdown in the assumptions of biologically-based reconstructions, or some combination of both. Having independent pre-Holocene temperature records in the European Alps that are mechanistically governed by different processes would therefore help in assessing the cause of the current proxy-model discrepancies.

Cosmogenic noble gas paleothermometry is a new geochemical technique for reconstructing past Earth surface temperatures (Tremblay et al., 2014a). Cosmogenic nuclides are produced by nuclear interactions between target atoms and high-energy cosmic-ray particles, both in Earth's atmosphere and in the solid Earth. Because the flux of secondary cosmic-ray particles decreases exponentially with depth in rock, production of cosmogenic nuclides is restricted to the uppermost few meters of the Earth's crust. The near surface production of rare nuclides such as ^{10}Be and ^{26}Al by cosmic-ray particle interactions in common rock-forming minerals like quartz has been extensively developed and utilized over the last 25 years by the geomorphology community to date the surface exposure of rocks and quantify erosion rates (e.g., Granger et al., 2013). Rare noble gas nuclides such as ^3He and ^{21}Ne are also produced in minerals by cosmic-ray particle

interactions. In common minerals like quartz and feldspars, these noble gases sometimes exhibit diffusive loss at Earth surface temperatures (Shuster and Farley, 2005; Gourbet et al., 2012; Tremblay et al., 2014b, 2017) and thus have not been widely utilized in cosmogenic nuclide studies. However, cosmogenic noble gas–mineral pairs exhibiting open-system behavior (simultaneous production and diffusion) can be utilized to reconstruct the temperatures that rocks experience while exposed to cosmic-ray particles at Earth’s surface when paired with observations of a quantitatively retained cosmogenic nuclide. In high latitude and/or high altitude environments, theoretical calculations indicate that measurements of ^3He in quartz can record temperature variations from the last glacial period to the present (Tremblay et al., 2014a).

Here, we apply cosmogenic noble gas paleothermometry to investigate temperatures recorded by cosmogenic noble gases since the LGM in the Gesso Valley, located in the southernmost Maritime Alps of Italy approximately 40 km from the Gulf of Genoa in the Mediterranean Sea (Fig. 1). The Gesso Valley was glaciated during the last glacial period. Glacial moraines and other geomorphic features have been mapped throughout the basin (Federici et al., 2003), and cosmogenic ^{10}Be exposure ages have been determined for boulders from three nested moraines that span from the LGM to the Younger Dryas cold period (YD) (Federici et al., 2008, 2012, 2017). A number of younger, Holocene-age moraines are preserved at higher elevations in the Gesso Valley (Fig. 1), and small glaciers restricted to the highest elevation cirques persist today (Federici et al., 2017). We measured cosmogenic ^3He abundances in quartz from a subset of the boulders with ^{10}Be exposure ages from the three previously-studied moraines. We also conducted stepwise degassing experiments to quantify the kinetics of ^3He diffusion in quartz from these boulders. Because

cosmogenic ^3He is simultaneously produced and diffusively lost during exposure in the moraines, the ‘apparent’ exposure ages we calculate from the measured ^3He abundances are younger than the ‘true’ exposure age determined from the ^{10}Be measurements. The difference between the ‘apparent’ and ‘true’ exposure ages can be used to calculate the integrated effective diffusion temperature (EDT) during exposure. This integrated EDT is the temperature corresponding to the mean diffusivity over a variable temperature history, and is therefore a function of the ambient temperature history (Tremblay et al., 2014a). Paired with sample-specific ^3He diffusion kinetics, we use the difference between ‘apparent’ and ‘true’ exposure ages to model the permissible integrated EDTs, and by relation temperature histories, of each boulder. The presence of numerous moraines with different exposure ages within the same valley is advantageous because it allows us to obtain temperature records over different time intervals for an area with a shared climate history.

METHODS

Of the Gesso Valley boulders for which ^{10}Be measurements exist, we obtained archived material (either whole rock or crushed, sieved fractions) from five samples for cosmogenic ^3He measurements: one from the Piano del Praiet moraine (PDP10), two from the Ponte Murato moraine (PM1, and PM4), and two from the Tetti del Bandito moraine (TDB1 and TDB3; Fig. 1 and Table 1). The ^{10}Be concentration in quartz for PDP10 ($223.8 \pm 9.6 \times 10^3$ atoms/g, using the $^{10}\text{Be}/^9\text{Be}$ of Nishiizumi et al. (2007) for NIST SRM4325) was measured at the Scottish Universities Environmental Research Centre Cosmogenic Isotope Analysis Facility in 2013; all other ^{10}Be concentrations are previously published (Federici et al., 2008, 2012). The ^{10}Be exposure ages of these boulders and other boulders from the same moraines have been used to associate the Piano

del Praiet, Ponte Murato, and Tetti del Bandito moraines with the Younger Dryas cold period, an intermediate cold period referred to locally as the Bühl stadial at ~18 ka, and the LGM respectively (Federici et al., 2008, 2012). We separated quartz from other phases using standard crushing, sieving, and magnetic methods, followed by a ‘frothing’ technique commonly used in the ceramics industry to separate quartz from feldspars in the largest sieve fraction that lacked composite grains (Buckenham and Rogers, 1954). Purified quartz was then used to both measure cosmogenic ^3He abundances and determine sample-specific ^3He diffusion kinetics. All helium isotope measurements were made with an MAP 215-50 sector field mass spectrometer in the BGC Noble Gas Thermochronometry Lab. Gas purification techniques and mass spectrometer analyses are as described in Tremblay et al. (2014b).

For cosmogenic ^3He measurements, 100–500 mg aliquots of quartz were weighed and packed into tantalum metal cups with both ends crimped, placed under vacuum in a sample chamber, and heated with a feedback-controlled 150 W diode laser to either 500, 800, or 1100 °C for 15 minutes until subsequent extractions yielded He signals indistinguishable from the instrumental detection limit. Empty tantalum cup blanks, heated to the same temperatures as the samples, and room temperature procedural blanks were measured throughout each analytical session and subtracted from the sample measurements; ^3He blank corrections were typically $2\text{--}3 \times 10^4$ atoms. Aliquots of air and ^3He -spiked helium standards of different manometrically-calibrated pipette volumes were analyzed throughout an instrumental tuning period and used to determine helium sensitivities; sensitivities varied linearly over the pressure range of the sample analyses, estimated by the size of the ^4He signal. We propagated uncertainties from the blank corrections and sensitivity

198 regression into the cosmogenic ^3He concentrations. We assume that all ^3He is cosmogenic, as any
199 magmatic ^3He present at the time of mineral formation or nucleonic ^3He (from the reaction $^6\text{Li}(n,$
200 $\alpha)^3\text{H}$) produced before reaching the near-surface is expected to be lost by diffusion (e.g., Tremblay
201 et al., 2014b), and any nucleogenic ^3He produced at the surface temperatures will likely be
202 negligible compared to cosmogenic ^3He (Lal, 1987).

203
204 To determine sample-specific diffusion kinetics, we conducted stepwise degassing experiments on
205 a proton-irradiated quartz grain from each sample. Proton irradiation generates a uniform
206 distribution of ^3He in quartz through similar nuclear reactions to those induced by cosmic ray
207 particles but with ten orders of magnitude or higher production rates, enabling step degassing
208 diffusion experiments to be conducted on single irradiated quartz grains (Shuster et al., 2004;
209 Shuster and Farley, 2005; Tremblay et al., 2014b). We conduct experiments on single grains rather
210 than multi-grain aliquots because it allows us to rapidly achieve and then maintain a spatially
211 homogeneous set point temperature, a critical requirement for step degassing experiments.
212 Previous work (Tremblay et al., 2014b) demonstrates that these single grain experiments are
213 reproducible for different quartz grains from the same sample. Quartz aliquots were irradiated with
214 a 228.5 MeV proton beam for 6 hours at the Francis H. Burr Proton Therapy Center at the
215 Massachusetts General Hospital in December 2015; the total proton fluence for this irradiation was
216 $9.14 \times 10^{15} \text{ p/cm}^2$. The irradiation target design and setup are detailed in Tremblay et al. (2017).
217 Proton irradiated quartz aliquots were examined with a binocular microscope, and single crystals
218 lacking visible penetrative fractures and inclusions (fluid or mineral) were selected for stepwise
219 degassing. The dimensions of the chosen grains were measured to estimate the spherical

equivalent radius used in later calculations to scale the diffusion lengthscale. Details of the stepwise degassing setup and helium measurements are described in Tremblay et al. (2014b).

In addition to determining the spherical equivalent radius of the quartz grains used in diffusion experiments, we also determined the spherical equivalent radii of the quartz grains used for cosmogenic measurements and assessed whether these radii are representative of the quartz size distribution in whole rock. Such an assessment is important because if we significantly reduced the grain size of quartz during the crushing process, this could lead to both an underestimation of the diffusion lengthscale to which the diffusion experiment size is scaled and missing cosmogenic ^3He from our measurements. First, we photographed and measured the dimensions of at least 100 quartz grains from the sieve fraction of each sample used for cosmogenic ^3He measurements. We determined major, intermediate, and minor axes of best fitting ellipsoids using the software ImageJ (Schneider et al., 2012) and calculated the radius of a sphere with the same surface area to volume ratio for each grain. We compared the spherical equivalent radii calculated using this approach to spherical equivalent radii determined from micro x-ray computed tomography (CT) analyses on a smaller number of grains from the same samples, wherein the grains were mapped in three dimensions with a resolution better than 5 micrometers. CT scans were obtained on the Xradia MicroXCT scanner at the University of Texas at Austin High-Resolution X-ray CT Facility and processed using the software Blob3D (Ketcham, 2005) as described in Tremblay et al. (2017). This comparison demonstrates that the ellipsoid approach consistently overestimates the spherical equivalent radius by ~50%, likely because the ellipsoid method significantly underestimates the surface area of grains. We therefore scaled the spherical equivalent radii from loose grain

measurements by a factor 1.5; the distribution of grain sizes from these measurements are shown in Fig. 2. Also shown in Fig. 2 is the probability distribution of spherical equivalent radii of quartz grains in whole rock. To determine this distribution, we determined circular equivalent radii from measured sectional areas of at least 100 quartz grains in thin sections, and inverted the distribution of circular equivalent radii to a distribution of spherical equivalent radii using the code STRIPSTAR and the methodology described by Heilbronner and Barrett (2013). For PDP10, the thin section was made from the same sample as the sample crushed for cosmogenic ^3He measurements. For the PM and TDB moraines, no whole rock material from the original samples was preserved; we therefore collected additional material from boulders exposed atop each of these moraines for thin sections, and assume that the grain size observed in these samples is representative of the samples for which we have cosmogenic ^3He data.

For all samples, the distribution of spherical equivalent radii for the sieve fraction has a smaller standard deviation than the radii determined from thin section measurements (Fig. 2), which is not surprising given that the sieving process removes larger and smaller grains. With the exception of the PM samples, we find that the mean spherical equivalent radius of quartz in the sieve fraction is equal to or slightly greater than the mean radius determined from thin section measurements (Fig. 2). The mean quartz radius in the sieve fraction from the PM samples is only slightly smaller than the mean radius from thin section measurements, and the two distributions show significant overlap. Given the good agreement between mean spherical equivalent radii for the sieve fraction and thin section quartz, we assume that the grain size has not been substantially reduced by sample crushing and use the mean and standard deviation of the sieve fraction radii distributions as the

appropriate diffusion lengthscale for modeling the diffusion of cosmogenic ^3He in each sample.

RESULTS

We report measured abundances of cosmogenic ^3He in quartz aliquots from each of the Gesso Valley samples in Table 2. We used version 3 (v3) of the online exposure age calculator code, a more recent version of the code published in Balco et al. (2008) that implements the cosmogenic ^3He production rate in quartz determined by Vermeesch et al. (2009), to calculate an apparent exposure age from the measured ^3He abundance in each aliquot. We assume that the erosion rate is negligible for all boulders sampled, as was assumed in the original publications reporting ^{10}Be exposure ages from these boulders (Federici et al., 2008, 2012). Sample coordinates, elevations, thicknesses, and shielding correction factors used in exposure age calculations are reported in Table 1. In Table 3, we report the weighted mean apparent ^3He exposure age for each sample determined using the scaling scheme of Stone (2000). We also recalculated the ^{10}Be exposure ages, normalizing the ^{10}Be concentrations to the isotope ratio standards of Nishiizumi et al. (2007), using v3 of the online exposure calculator with version 1.1 of the muogenic production rate code and the CRONUS-Earth calibration data set for ^{10}Be production rate (Borchers et al., 2016), and using the scaling scheme of Stone (2000) (Table 3). Our choice to use the global ^{10}Be production rate calibration dataset in Borchers et al. (2016) over a local ^{10}Be production rate calibration (Claude et al., 2014) does not substantially influence the results presented herein. Because the production rates of ^3He and ^{10}Be in quartz are not determined from the same calibration datasets, we use the external uncertainties in exposure ages in all calculations that follow. We divided the weighted mean apparent ^3He exposure ages by the ^{10}Be exposure ages (both with external uncertainties) to

calculate ^3He retention, which represents the fraction of cosmogenic ^3He produced during surface exposure that remains in the quartz analyzed (Tremblay et al., 2014a).

Fig. 3 shows ^3He retention as a function of exposure duration in the five samples we analyzed. All Gesso Valley samples retain less than 50% of the cosmogenic ^3He that was produced during their exposure (Table 3, Fig. 3). Retention generally decreases with increasing exposure duration: quartz from PDP10, sampled from the highest elevation moraine with an exposure age of 14071 ± 1220 years, retains 46% of its cosmogenic ^3He , while quartz from TDB1, sampled from the lowest elevation moraine with an exposure age of 23397 ± 2072 years, retains only 6% of its cosmogenic ^3He . In cases where we have multiple samples from the same moraine, we observe significant intra-moraine differences in ^3He retention. PM1 and PM4, both from the Punto Murato moraine with exposure ages of 16356 ± 1023 and 19213 ± 799 years, respectively, have ^3He retentions of 0.28 ± 0.04 versus 0.36 ± 0.04 (Table 3, Fig. 3). Similarly, the two Tetti del Bandito moraine samples TDB1 and TDB3, with exposure ages of 23397 ± 1085 and 21003 ± 965 , respectively, have ^3He retentions of 0.06 ± 0.01 versus 0.29 ± 0.04 (Table 3, Fig. 3).

In order to (1) calculate effective diffusion temperatures (EDTs) and infer temperature histories from the observed ^3He retention in quartz from each sample, and (2) assess the differences in ^3He retention between samples from the same moraine, we need to know the diffusion kinetics of ^3He in each sample. Fig. 4 shows the results of step degassing experiments on proton-irradiated quartz from the Gesso Valley samples in Arrhenius plots where the natural log of diffusivity, calculated from the cumulative fraction of gas released during each heating step (Fechtig and Kalbitzer,

1966), is plotted as a function of inverse temperature (gray circles).

All Gesso Valley quartz samples exhibit some degree of nonlinearity in the Arrhenius plots (Fig. 4). While we do not have a mechanistic explanation or model for this type of complex diffusion behavior (Tremblay et al., 2014b), multiple diffusion domain (MDD) models (Lovera and Richter, 1989; Harrison et al., 1991; Lovera et al., 1991) can reproduce the nonlinearity observed in laboratory degassing experiments and appear to be relevant to ^3He diffusive loss over 10^3 – 10^4 year timescales, as demonstrated for a geologic case study for which the temperatures during surface exposure are reasonably well known (Tremblay et al., 2014b). We constructed MDD models optimized to fit each of the helium step degassing experiments on Gesso Valley quartz samples following the approach outlined in Tremblay et al. (2017). Fig. 5 shows the misfit between the calculated diffusivities from MDD models and the experimentally-determined diffusivities as a function of number of diffusion domains, where the misfit statistic was calculated as in Tremblay et al. (2017). The misfit shown for a given number of diffusion domains is the minimum misfit found after searching over a large range of model parameters (activation energy E_a , pre-exponential factor(s) D_0/a^2 , and gas fraction(s)).

We found that, for all five step degassing experiments, increasing the number of diffusion domains from 1 to 2 and from 2 to 3 significantly reduced the misfit between the observed diffusivities and those calculated with the MDD model (Fig. 5). However, increasing the number of diffusion domains from 3 to 4 did not significantly reduce the misfit between the observed and calculated diffusivities (Fig. 5). For experiment PM1-A, attempts at constructing a four domain model yielded

two domains with the same pre-exponential factor and thus are the equivalent of the three domain model. Therefore for all experiments we use the diffusion parameters corresponding to the optimized three domain model. Lines corresponding to the diffusion parameters of the three domains, as well as the calculated diffusivities for the three domain models, are shown in color over the experimentally determined diffusivities in Fig. 4. The activation energies, pre-exponential factors, gas fractions, and misfit statistic for these three domain models are reported in Table 4.

As discussed in Section 2, we need to scale the diffusion kinetics determined from the step degassing experiments to the diffusion lengthscale appropriate for the cosmogenic ^3He abundance measurements. In constructing MDD models, we cannot independently parameterize the diffusivity at infinite temperature, D_0 , and the diffusion lengthscale, a . Instead, we model them together as the natural logarithm of the pre-exponential factor in the Arrhenius expression, $\ln(D_0/a^2)$, which in an Arrhenius plot corresponds to the y-intercept. Because we cannot independently model the diffusion lengthscale a , we must make an assumption about how to scale the MDD models appropriately. This is not a problem for the $^{40}\text{Ar}/^{39}\text{Ar}$ thermochronometry community in which MDD models were developed, because in almost all cases argon diffusion kinetics and naturally-occurring argon isotope abundances are measured in the same mineral grain (e.g., Lovera et al., 1997/8). Here, we assume that the diffusion lengthscale of all domains, and by inference all the pre-exponential factors in a given MDD model, scales with the spherical equivalent radius of the quartz grain analyzed. Theoretically, this implies that diffusion lengthscale of the most retentive domain (the domain with the lowest $\ln(D_0/a^2)$ or intercept in Arrhenius space) is the spherical equivalent radius of the grain analyzed. Practically, this scaling is accomplished as

follows:

$$\left(\frac{D_0}{a^2}\right)_{scaled} = \left(\frac{D_0}{a^2}\right)_{MDD} \left(\frac{a_{sde}^2}{a_{cosmo}^2}\right) \quad (1)$$

where a_{sde} is the spherical equivalent radius of the step degassing experiment quartz grain and a_{cosmo} is the spherical equivalent radius of the quartz grains used for the cosmogenic ^3He measurements (Fig. 2).

With the scaled, sample-specific diffusion kinetics, we explore possible temperature scenarios to explain the observed cosmogenic ^3He abundances in the Gesso Valley samples. To do this, we use forward models of simultaneous production and diffusion to model how cosmogenic ^3He retention evolves as a function of exposure duration under different temperature scenarios. We begin with the simplest possible scenario of constant temperature over time. Although constant temperatures are not climatologically realistic, this calculation allows us to determine the EDT, which is the temperature corresponding to the mean diffusivity for a given temperature history, that is consistent with the observed cosmogenic ^3He retention of each sample. These EDTs are equal to or greater than the true mean temperatures the samples experienced over their exposure durations because of the nonlinear relationship between diffusivity and temperature (Tremblay et al., 2014a). Fig. 6 shows the evolution of ^3He retention as a function of exposure duration for constant temperature scenarios in 2 °C increments from 0 °C to 30 °C. These retention evolution curves differ for each Gesso Valley quartz sample for several reasons: (1) each sample has a different set of diffusion kinetics, assuming a three domain diffusion model (Fig. 4, Table 4), (2) these sample

specific diffusion kinetics are scaled to different spherical equivalent radii based on the measured grain size distributions of quartz in the sieve fraction used for cosmogenic ^3He measurements (Fig. 2), and (3) the cosmogenic ^3He production rate in quartz differs between samples. In each panel of Fig. 6 we report the integrated EDT that agrees with the observed cosmogenic ^3He retention in each quartz sample. We provide two uncertainty estimates on this integrated EDT. One set of EDT uncertainties in parentheses accounts for the uncertainty in ^3He retention and exposure duration as determined from ^{10}Be measurements; the second set of uncertainties also accounts for uncertainty in the spherical equivalent radius to which the experimentally-determined diffusion kinetics are scaled.

The most readily observable feature of the models in Fig. 6 is that the integrated EDT calculated for each quartz sample is different. This is in part expected because the different moraines represented by these samples are located at different elevations in the Gesso Valley, and thus will experience different temperatures at any point in time due to the atmospheric lapse rate. This may also in part be due to the samples having different exposure durations; for example, a change in temperature between the deposition of the TDB moraine and the PM moraine would only be reflected in the cosmogenic ^3He retention and integrated EDT of the TDB moraine samples. Differences in integrated EDT between samples from the same moraine, on the other hand, are unexpected. For PM1 we calculate an integrated EDT of 7.6 °C, while for PM4 we calculate a much higher integrated EDT of 19.7 °C. Similarly, for TDB1 we calculate an integrated EDT of 24.5 °C, while for TDB3 we calculate a much lower integrated EDT of 15.8 °C. These intra-moraine discrepancies preclude a straightforward inversion for changes in EDT through time in

the Gesso Valley from the inter-moraine differences in ^3He retention. We explore possible causes for these intra-moraine discrepancies in the discussion section; here, we compare our observations to modern and paleoclimate observations and simulations to assess whether the EDTs we calculate are plausible for the Gesso Valley since the LGM.

To contextualize these EDTs integrated over the exposure duration of each sample, in Fig. 7 we use modern daily temperature records from 2002 to 2016 to calculate present-day mean temperatures (solid lines) and EDTs (dashed lines) at the elevation of each moraine. We might expect present-day EDTs at each moraine to be comparable to or greater than the EDT integrated over the samples' exposure durations, considering that mean temperatures during the early, pre-Holocene exposure history of each sample were likely lower than today. However, this expectation may be overly simplistic, as changes in the amplitude of daily and seasonal temperatures since the LGM will also affect the integrated EDTs. Nonetheless, calculation of modern EDTs provides an estimate for the magnitude of the difference between mean temperatures and EDTs due to temperature variations on daily and seasonal timescales in the Gesso Valley.

We obtained temperature records at the elevation of each moraine by scaling daily mean, minimum, and maximum temperature data from two meteorological stations within the Gesso Valley: Diga della Piastra (44.227 °E, 7.389 °N, 959 m) and Diga del Chiotas (44.168 °E, 7.334 °N, 1980 m). These data are publicly available through the Environmental Protection Agency for the Piemonte Region (arpa.piemonte.gov.it). We scaled the temperature data at Diga della Piastra to the elevation of the TDB and PM moraines and the temperature data at Diga del Chiotas to the

elevation of the PDP moraine using monthly average lapse rates determined from the same dataset (minimum = 2.8 °C/km in December/January; maximum = 6.7 °C/km in May), and calculated the modern EDT using these scaled temperature data and the activation energies of the best fit MDD models in Fig. 4 and Table 4. The modern EDTs at the three moraine elevations are ~4–5 °C greater than the mean temperatures, reflecting the effect of daily and seasonal temperature amplitudes on the mean diffusivity and EDT. We do not observe a consistent relationship between modern EDT, calculated at the elevation of each moraine, and integrated EDTs calculated for each sample. For PM4 and TDB1, the modern EDT estimate (15.1 and 15.9 °C) is several degrees lower than the EDT integrated over each sample's exposure duration (19.7 +3.5/–3.7 and 24.5 +4.3/–3.9 °C). In contrast, the modern EDT estimates for PDP10 and TDB3 (9.8 and 15.9 °C) are comparable to the EDTs integrated over their exposure durations (13.8 +4.3/–5.7 and 15.8 +3.9/–4.5 °C), and for PM1 the modern EDT estimate (15.0 °C) is several degrees higher (vs. 7.6 +3.5/–3.4 °C).

In addition to comparing the integrated EDTs calculated from observed cosmogenic ³He abundances to modern day EDTs in the Gesso Valley, we can compare our cosmogenic ³He observations to those that would result from (1) temperature histories simulated in general circulation models (GCMs), and (2) temperature reconstructions based on other proxies at nearby locations. GCM simulations and independent proxy reconstructions provide more realistic late Quaternary temperature scenarios with which to test the plausibility of our cosmogenic ³He observations. As cosmogenic noble gas paleothermometry is refined and improved, cosmogenic ³He observations may also be useful for assessing the fidelity of these paleoclimate simulations and reconstructions based on other proxies. For both model and proxy comparisons, the

temperature history used to model cosmogenic ^3He abundances must be equal in duration to the moraine sample exposure.

Most GCM paleo-experiments simulate climate at a particular point in time, such as the mid-Holocene or LGM; only a handful of GCMs simulations have explored transient climate evolution in the Holocene and latest Pleistocene. Here, we model how cosmogenic ^3He retention would evolve as a function of exposure duration using seasonal temperature outputs from the TraCE-21ka transient simulation. TraCE-21ka uses the National Center for Atmospheric Research (NCAR) Community Climate System Model version 3 (CCSM3), a synchronously coupled atmosphere-ocean general circulation model (GCM) (Collins et al., 2006), to simulate the Earth's climate from the LGM (22 thousand years ago) to the present (Liu et al., 2009; He, 2011). We obtained mean and maximum seasonal (DJF, MAM, JJA, and SON) temperatures from the TraCE-21ka simulation for the 44.3 °N, 7.4 °E grid cell including the Gesso Valley. We chose mean and maximum seasonal temperatures for practical reasons (sub-seasonal temporal resolution is computationally unwieldy), but also because these represent endmember EDT scenarios for the moraines in Gesso Valley. Mean seasonal temperatures represent the low-EDT endmember, as this scenario implies that the mean temperatures represent the full amplitude of seasonal temperature variation and that there is no sub-seasonal (e.g., daily) variability. Maximum seasonal temperatures represent the high-EDT endmember, as this scenario implies that the maximum sub-seasonal temperature simulated during a three month interval is the temperature over the duration of that season. We thus expect the observed cosmogenic ^3He retention in our samples to be bracketed by the predicted cosmogenic ^3He retention from these endmember scenarios, with the mean seasonal

temperature scenario placing an upper bound on cosmogenic ^3He retention and the maximum seasonal temperature placing a lower bound.

TraCE-21ka simulation temperatures were determined for a mean elevation above sea level for the grid cell, which changed through the simulation as simulated sea level changed. However, the elevation of our sample sites with respect to sea level would have also changed through time, meaning that the relative offset between our sample site elevation and the mean grid cell elevation would have remained constant. We therefore scale the TraCE-21ka simulation temperatures to our sample sites using the present day difference between the sample site elevations and TraCE-21ka mean elevation assuming the modern seasonal lapse rate determined from the meteorological stations discussed above. The atmospheric lapse rate in the Gesso Valley likely changed between the LGM and the present, especially considering the fact that the valley was more extensively glaciated during part of this interval. Nonetheless, we assume the modern rate because (1) we have no independent means for assessing how different paleo-lapse rates may have been, and (2) any differences from the modern lapse rate when the valley was glaciated were likely $\leq 2\text{ }^\circ\text{C/km}$ (e.g., Davis et al., 2003; Gardner et al., 2009; Loomis et al., 2017), which will not be resolvable using our cosmogenic noble gas observations that span $\leq 1\text{ km}$ in elevation (Tremblay et al., 2014a).

For all Gesso Valley quartz samples, the observed cosmogenic ^3He retention is bracketed by the ^3He retention calculated assuming mean seasonal temperatures and the ^3He retention calculated assuming maximum seasonal temperatures scaled from the TraCE-21ka simulation. For PDP10 (Fig. 8), PM4 (Fig. 9), and TDB1 (Fig. 10), we calculate cosmogenic ^3He retention from the

TraCE-21ka simulation maximum seasonal temperature that is in agreement within uncertainty with the observed retention in these samples. Cosmogenic ^3He retention calculated from the TraCE-21ka mean seasonal temperatures agrees with the observed cosmogenic ^3He retention in PM1 within uncertainty (Fig. 9), while for TDB3 the observed cosmogenic ^3He retention lies between that predicted from the mean and maximum seasonal TraCE-21ka temperatures.

We also use chironomid-based July temperature reconstructions from other Alpine locations to model cosmogenic ^3He retention for comparison with our cosmogenic ^3He observations. The advantage of chironomid reconstructions is that we can splice together records from several locations to obtain coeval coverage with samples PDP10 and PM1, which have the youngest ^{10}Be exposure ages of 14071 ± 1220 and 16356 ± 1601 years, respectively. The lack of Alpine chironomid records before 16 cal. years BP prevents us from using chironomid-based July temperature reconstructions to model cosmogenic ^3He retention in PM4, TDB1, and TDB3. Similarly, temperatures reconstructions from other Alpine proxy records do not have sufficient continuous temporal coverage for use in models of cosmogenic ^3He retention for our samples. Like the maximum seasonal temperatures from the TraCE-21ka simulation, we treat the mean July temperature inferred from chironomids as a high-EDT endmember scenario, as this scenario implies that the mean July temperature is representative of sub-annual temperatures.

The most proximal chironomid-based mean July temperature reconstruction is from Lago Piccolo di Avigliana (LPA), located in the Italian Alps ~80 km north of the Gesso Valley (45.05 °N; 7.38 °E, 365 m), where the record extends from 14200 to 9500 cal. year BP (Larocque and Finsinger,

2008). In order to obtain coeval coverage with the exposure ages of PDP10 and PM1, we spliced the LPA record with chironomid July temperature reconstructions from: Schwarzsee ob Sölden (SOS), a high-alpine lake in the Austrian Alps (46.96583 °N, 10.94611 °E, 2796 m) with a chironomid record from 10200 to –36 cal. years BP (Ilyashuk et al., 2011); Lac Lautrey (LAU), a small lake in the French Jura Mountains (46.58722 °N, 5.86389 °E, 788 m) with a chironomid record from 15908 to 11033 cal. years BP (Heiri and Millet, 2005); and Hinterburgsee (HIN), a subalpine lake in the northern Swiss Alps (46.71833 °N, 8.06750 °E, 1515 m) with a chironomid record from 12210 to 1900 cal. years BP (Heiri et al., 2004). Like the GCM simulation, we scaled the July temperature reconstructions from each location to the elevations of PDP10 and PM1 using modern lapse rate information, and when temporal overlap occurred between two or more chironomid records we used an average of the scaled temperatures weighted by the inverse distance between the chironomid sites and our study site.

In Figs. 8 and 9 we show the scaled, spliced July temperature reconstruction using all four chironomid records and the corresponding model for cosmogenic ³He retention in PDP10 and PM1, respectively. We found that different chironomid record splices (e.g., SOS + LPA; SOS + HIN + LPA; SOS + LPA + LAU; SOS + HIN + LPA + LAU) result in very small differences in modeled cosmogenic ³He retention; therefore only the four record splice (SOS + HIN + LPA + LAU) is shown. Like the maximum seasonal temperatures from the TraCE-21ka simulation, we model cosmogenic ³He retention from the mean July temperature reconstruction that agrees with our observations from PDP10 and that underestimates the observed ³He retention in PM1.

DISCUSSION

To a first order, the fact that cosmogenic ^3He retention calculated with endmember temperature scenarios from a GCM simulation and an independent proxy reconstruction brackets our cosmogenic ^3He observations indicates that the ^3He observations record ambient temperatures with some accuracy. The observation that our integrated EDTs are not tens of degrees different from modern EDTs in the Gesso Valley calculated with meteorological data also indicates accuracy, as temperature differences between the present-day and LGM were unlikely to exceed 15 °C (e.g., Becker et al., 2016), and post-LGM temperature differences were likely to be much smaller. This first order agreement suggests that our cosmogenic ^3He measurements are providing meaningful information on ambient temperature conditions during exposure. For example, we do not calculate integrated EDTs below 0 °C, as we do for cosmogenic ^3He measurements made on Holocene-age glacial erratics in Antarctica (Tremblay et al., 2014a), nor do we calculate integrated EDTs unfeasibly high for Earth surface conditions (e.g, EDTs of 70–80 °C that we obtain for the Moon (Shuster and Cassata, 2015)). However, for the purposes of reconstructing past climate variations, the substantial intra-moraine differences in EDTs are problematic, precluding us from carrying out a straightforward inversion for changes in EDT through time in the Gesso Valley from the inter-moraine differences in ^3He retention. For both the PM and TDB moraines, the difference in integrated EDTs between samples from the same moraine is ~10 °C. These intra-moraine differences require explanation.

One possibility is that these intra-moraine temperature differences are real and reflect differential shading of the samples by vegetation, snow cover or topography. For example, patchy vegetation

on a moraine crest may cause one boulder to be fully shaded under a tree canopy, while another boulder tens of meters away remains unshaded. Similarly, boulders nearby to one another might accumulate substantial or insignificant snow cover depending on their relative positioning and shielding from prevailing winds during the wintertime. Unshaded rock samples can experience significantly higher daytime temperatures due to insolation than shaded samples. As discussed in Tremblay et al. (2014a), heating of rocks due to incident solar radiation can substantially raise rock temperatures above daily maximum air temperatures. Amplification of temperatures 5–10 °C above the daily maximum is common in non-desert environments (McGreevy, 1985; Hall et al., 2005; Bartlett et al., 2006; Schwarz et al., 2012). Considering our modern EDT calculations from meteorological station data, if we increase the maximum daily temperature by 5 or 10 °C, we find significant increases in the EDT. For example, using the diffusion kinetics for TDB1, by increasing the maximum daily temperature in the meteorological data by 5 °C, we find that EDT increases from 15.9 to 19.2 °C. Increasing the maximum daily temperature by 10 °C increases the EDT to 23.0 °C, which is within the uncertainty of the EDT integrated over TDB1's exposure duration. Therefore it is possible that, in the case of the TDB moraine, TDB3 may have been shaded or snow covered during part of its exposure history, while TDB1 was fully exposed to incoming solar radiation throughout its exposure. Similarly, PM1 may have been shaded by vegetation or snow covered during periods of time when PM4 was not.

This interpretation is consistent with the comparison of observed cosmogenic ^3He retention to calculated retention from TraCE-21ka and chironomid temperatures. Observations from PDP10, PM4, and TDB1 are closest to the TraCE-21ka simulation maximum seasonal temperature

calculations, while observations from PM1 are closer to the calculations with the mean seasonal temperature and observations from TDB3 lie between the predicted ^3He retention from mean and maximum seasonal temperature scenarios. We would expect mean temperatures to agree with our cosmogenic ^3He observations, as is the case for PM1, if no heating due to insolation occurred. Following the same reasoning, we anticipate that samples experiencing nonzero insolation will have cosmogenic ^3He abundances that are lower than what is expected from mean air temperatures, as is the case for PDP10, PM4, TDB1, and TDB3. Likewise, the apparent agreement between the observed cosmogenic ^3He retention in PDP10 and the chironomid-based reconstruction of mean July temperatures, which will be significantly greater than mean temperatures throughout most of the year, supports the interpretation that the temperatures experienced by sample PDP10 exceeded air temperatures during its exposure to cosmic ray particles. A more precise relationship between insolation-induced daily rock temperature amplifications and maximum seasonal air temperatures or mean July air temperatures could be obtained by monitoring *in situ* rock temperatures adjacent to meteorological stations, such that these temperature scenarios could be adjusted and provide more information than just a high-EDT endmember.

We note that shading from solar radiation and shielding of cosmic rays are not equivalent. Vegetative cover can have a substantial effect on heating by insolation, but in most cases a negligible effect on cosmogenic nuclide production rates due to its relatively low density. Similarly, thin snow cover will not substantially affect cosmogenic nuclide production rates but will cause rock temperatures to differ substantially from air temperatures. Thick snow cover (≥ 1 m) will affect both production rates and temperatures. Today, there is significant vegetation cover

on the TDB and PM moraines, but no cover at PDP. Unfortunately, we have no way of assessing the degree of vegetation cover on the TDB and PM moraines before the modern era, and no way to assess the past degree of snow cover for all moraines (although observations of in situ ^{14}C in quartz could help address snow cover; e.g., Hippe et al., 2014). Topography can shield rocks from cosmic ray particles, but these effects are accounted for in our calculations of cosmogenic nuclide production rates (Table 1); in contrast, we have not accounted for the effects of topographic shading on rock surface temperatures. We do not have detailed enough locations for the TDB and PM samples to identify the original boulders that were sampled and assess differences in topographic shading, although we suspect this would be secondary to vegetation and snow cover effects.

Another possible explanation for the intra-moraine differences is that our MDD model representations of helium diffusion kinetics in Gesso Valley quartz samples are inaccurate and/or inadequate. The MDD models we construct are inherently non-unique, and while the models we use minimize the misfit between the observed and calculated diffusivities in our step degassing experiments for a given number of domains, comparable fits can be achieved over a range of diffusion parameters. To illustrate this, in Fig. 11 we show minimized values of MDD model misfit, calculated using the misfit statistic defined in Tremblay et al. (2017), as a function of activation energy E_a for three domain models fit to each of the step degassing experiments shown in Fig. 4. For most of the step degassing experiments, there is a broad range of activation energies (and associated pre-exponential factors and gas release fractions) over which the misfit with the MDD model changes only slightly; these changes in misfit are much smaller than the change in

misfit associated with increasing the number of diffusion domains and the model complexity (Fig. 5).

For example, the MDD misfit for the PM1-A step degassing experiment ranges between 7.0 and 10.2% between activation energies of 80 and 97.5 *kJ/mol* (Fig. 11). The MDD diffusion kinetics we use in the forward models for PM1 quartz presented above assume an activation energy of 89.6 *kJ/mol*. If instead we use a different set of diffusion kinetics for a three domain model that yields a comparable misfit with the step degassing experiment ($E_a = 97.5$ *kJ/mol*; $\ln(D_0/a^2) = 12.2, 10.1, 16.8$; $f_{gas} = 0.45, 0.44, 0.11$; Misfit = 0.095), we calculate an integrated EDT from the cosmogenic ³He retention in PM1 quartz of 17.8 (± 2.3) +3.8/-3.9 °C, which is in agreement with the integrated EDT we calculated for PM4 (Fig. 6). This highlights how sensitive the temperatures we calculate from an observed amount of cosmogenic ³He retention are to the diffusion kinetics we use. While different MDD models might reproduce diffusivities observed in laboratory step degassing experiments comparably well, the downward extrapolation of these models results in significantly different diffusivities at the temperatures characterizing Earth's surface. This suggests that some or all of the intra-moraine differences in integrated EDTs could be attributed to uncertainties in how we extrapolate laboratory-determined diffusion kinetics. Given that we do not yet have a mechanistic understanding of what controls the complex noble gas diffusion behavior we observe in our experiments, discriminating between different MDD models of comparably good fit (and even assessing whether MDD models adequately represent the processes responsible for complex behavior) is difficult at this stage.

A third possible explanation for the intra-moraine variation could arise from our grain size analysis and scaling of MDD models. Uncertainty in the physical significance of our MDD models translates into an uncertainty in our assumptions about how to scale our MDD model fits from step degassing experiments to the cosmogenic ^3He measurements. However, because we have scaled the results of each experiment using the same assumptions in Eq. 1, the effects will be systematic. Similarly, the factor of 1.5 we applied to estimated spherical equivalent radii of quartz from the sieve fractions, based on different approaches to estimate surface area to volume ratios and ground truthing with x-ray computed tomography data, will have systematic effects on all integrated EDTs. Assuming that the MDD model scaling and correction applied to sieve fraction measurements are appropriate, we must also consider the possibility that our grain size analysis for the PM and TDB samples does not represent the actual grain size and diffusion lengthscale of quartz in these samples. Since we did not have whole rock material from the original PM and TDB samples, we made thin sections from other boulders collected from the PM and TDB moraines to compare with the size distributions of quartz in the sieved fraction. While there is good agreement between the mean spherical equivalent radii of quartz measured in these thin sections and in the sieve fractions, it is possible that in the original sample the mean quartz size before crushing was much larger. As a sensitivity test, we again use PM1 as an example. In order to obtain an integrated EDT for PM1 equivalent to that calculated for PM4 of 19.7 °C, we must increase the spherical equivalent radius assumed for the cosmogenic ^3He measurement by 110% (without changing the spherical equivalent radius for PM4). While such a dramatic underestimation of the PM1 grain size, and more generally >100% uncertainty in all our PM and TDB grain size analyses, seems unlikely, we cannot rule out such a possibility given that whole rock material from these samples

was unavailable.

As a final potential source of intra-moraine variation, the moraine boulders that we sampled may have more complex exposure histories than we allow for in our production and diffusion models, either due to cosmogenic ^{10}Be and ^3He inheritance or due to nonzero erosion rates that vary between boulders. More complex exposure histories are plausible for all three moraines, as the ^{10}Be exposure ages from a given moraine do not overlap within their internal uncertainties (Table 3). Although we only studied one boulder from the PDP moraine, cosmogenic ^{10}Be measurements for four additional PDP boulders also exhibit dispersion that cannot be explained by measurement uncertainty alone (Federici et al., 2008). PDP10, the sample studied here, has the oldest exposure age of the five boulders with ^{10}Be measurements. We do not have measurements of additional cosmogenic nuclides (e.g., *in situ* ^{14}C) to test whether our samples exhibit evidence for complex exposure. Nonetheless, we can explore what effects inheritance and nonzero erosion might have on our cosmogenic ^3He observations and the EDTs we calculate from them.

Inheritance would most likely affect the boulders from each moraine with the oldest apparent ^{10}Be exposure ages: PDP10, PM4, and TDB1. The cosmogenic ^3He observations from these boulders yield higher integrated EDTs than other boulders from the same moraine (in the case of PM4 and TDB1) and are closest to the ^3He retention calculated using the high-EDT endmember scenarios (maximum seasonal temperatures from TraCE-21ka and mean July temperatures from spliced chironomid records). In order for inheritance to explain these observations and the intra-moraine differences in integrated EDT, the quartz in these boulders would have to lose a substantial

proportion of their inherited ^3He relative to inherited ^{10}Be . This is not unreasonable considering that temperature-dependent diffusive loss would also affect cosmogenic ^3He produced prior to boulders being deposited in a moraine; thus we consider inheritance to be a viable option to explain some of the intra-moraine discrepancies we observe.

In contrast, nonzero erosion rates will likely affect the boulders from each moraine with the youngest apparent ^{10}Be exposure ages: PM1 and TDB3. The cosmogenic ^3He observations from these boulders yield lower integrated EDTs than other boulders from the same moraine and are closer to the ^3He retention calculated using the low-EDT endmember scenario (mean seasonal temperatures from TraCE-21ka). If we assume that 15 cm of material has been eroded since the initial exposures of PM1 and TDB3—corresponding to the depth at which daily temperature oscillations typically become negligible in rock (Tremblay et al., 2014a)—and that the exposure ages calculated from ^{10}Be measurements from PM4 and TDB1 are the respective true exposure ages, we can recalculate the ^{10}Be exposure age, ^3He apparent exposure age, and ^3He retention for PM1 and TDB3. This results in an increase in ^{10}Be exposure age (e.g., from 16356 ± 1023 to 18821 ± 1335 for PM1), but not a substantial decrease in ^3He retention (e.g., from 0.28 ± 0.04 to 0.25 ± 0.04 for PM1). As a consequence, the integrated EDTs we would calculate for these samples including the effects of erosion would not be substantially higher than those we calculated assuming no erosion. A similar effect is expected if, rather than erosion of the boulder surfaces themselves, the boulders were initially shielded by a variable thickness of sediment cover that has since eroded (e.g., Putkonen and Swanson, 2003; Heyman et al., 2011). Thus the effects of variable erosion seem unlikely to fully explain the intra-moraine differences we observe.

In summary, there is substantial intra-moraine variability in the integrated EDTs we calculate from our cosmogenic ^3He observations that requires explanation. We have outlined four major sources of uncertainty in our approach that could explain these intra-moraine variations. Ultimately, these potential sources of uncertainty are too under-constrained at this time to allow for a straightforward interpretation about the climate history of the Maritime Alps during deglaciation from our cosmogenic noble gas data. Nonetheless, we calculate integrated EDTs for all samples that are bracketed by plausible endmember EDT scenarios for the Gesso Valley based on mean and maximum seasonal temperatures from the TraCE-21ka simulation and on chironomid-derived mean July temperature reconstructions. The trend toward the high-EDT endmember scenarios for all samples except PM1 is not surprising, given that we expect integrated EDTs to exceed the mean ambient temperatures in a sample's exposure history because of the nonlinear dependence of diffusivity on temperature. The observation that our integrated EDTs are not drastically different from modern EDTs in the Gesso Valley is also encouraging, given the magnitude of plausible temperature differences between the LGM and today. Collectively, these results demonstrate promise for the application of cosmogenic noble gas paleothermometry in paleoclimate studies, provided that the four major sources of uncertainty we detail above are accounted for in future applications.

CONCLUSIONS

Integrated EDTs since the LGM in the Gesso Valley, calculated from our observations of cosmogenic ^3He concentrations in quartz, range from 8 to 25 °C and are consistent with what we

expect from modern meteorological station data, a GCM simulation of Earth's climate since the LGM, and data from independent proxies in the region. Nonetheless, there are nontrivial differences between the integrated EDTs we calculate, particularly for samples from the same moraine, that require explanation. We identify four major potential sources of uncertainty that could account for these discrepancies: (1) the fact that we have not accounted for variations in radiative heating of the boulder surfaces across samples due to differential shading, (2) limitations in our understanding of and ability to model and extrapolate helium diffusion kinetics when complex behavior is observed, (3) uncertainties associated with our quartz grain size analyses, and (4) unaccounted for erosion or cosmogenic inheritance. At this stage, all four of these possibilities could be contributing to intra-moraine and inter-moraine variability in reconstructed temperatures. Because of these uncertainties, and the fact that we have no cosmogenic ^3He observations from younger moraines that record only Holocene temperatures in the Gesso Valley, it is difficult to fully compare our results to the TraCE-21ka and chironomid temperature records, or to invert our results directly for changes in EDT through time in the Gesso Valley from the inter-moraine differences in ^3He retention. As a consequence, it is not yet possible to use these data to test the hypothesis that the post-LGM climate evolution and glacier dynamics of the Maritime Alps differed from other Alpine regions with our dataset. These results nonetheless demonstrate first order accuracy in the temperatures recorded by cosmogenic noble gas paleothermometry, and highlight major sources of uncertainty that can be addressed in future applications to improve how cosmogenic noble gas paleothermometry contributes to paleoclimate studies.

ACKNOWLEDGEMENTS

MMT and DLS acknowledge support from the NSF Petrology and Geochemistry Program (EAR-1322086 to DLS), the UC Berkeley Larsen Grant, and the Ann and Gordon Getty Foundation. MMT was supported by an NSF Graduate Research Fellowship. MS acknowledges support from the Royal Society (IE150603), the Leverhulme Trust (IAF-2016-001) and NERC (CIAF 9092.1010). AR acknowledges support from the University of Pisa fund PRA (2017). We thank Associate Editor Kathleen R. Johnson, Jakob Heyman, and an anonymous reviewer for constructive feedback on this work.

REFERENCES CITED

- Annan, J.D., Hargreaves, J.C., 2013. A new global reconstruction of temperature changes at the Last Glacial Maximum. *Climate of the Past* 9, 367–376.
- Annan, J.D., Hargreaves, J.C., 2015. A perspective on model-data surface temperature comparison at the Last Glacial Maximum. *Quaternary Science Reviews* 107, 1–10.
- Balco, G., Stone, J.O., Lifton, N.A., Dunai, T.J., 2008. A complete and easily accessible means of calculating surface exposure ages or erosion rates from ^{10}Be and ^{26}Al measurements. *Quaternary Geochronology* 3, 174–195.
- Bartlein, P.J., Harrison, S.P., Brewer, S., Connor, S., Davis, B., Gajewski, K., Guiot, J., Harrison-Prentice, T.I., Henderson, A., Peyron, O., Others, 2011. Pollen-based continental climate reconstructions at 6 and 21 ka: a global synthesis. *Climate Dynamics* Springer 37, 775–802.
- Bartlett, M.G., Chapman, D.S., Harris, R.N., 2006. A decade of ground–air temperature tracking

at Emigrant Pass Observatory, Utah. *Journal of Climate* 19, 3722–3731.

Becker, P., Seguinot, J., Jouvet, G., Funk, M., 2016. Last Glacial Maximum precipitation pattern in the Alps inferred from glacier modelling. *Geographica Helvetica* 71, 173–187.

Blaga, C.I., Reichert, G.-J., Lotter, A.F., Anselmetti, F.S., Sinninghe Damsté, J.S., 2013. A TEX 86 lake record suggests simultaneous shifts in temperature in Central Europe and Greenland during the last deglaciation. *Geophysical research letters* 40, 948–953.

Borchers, B., Marrero, S., Balco, G., Caffee, M., Goehring, B., Lifton, N., Nishiizumi, K., Phillips, F., Schaefer, J., Stone, J., 2016. Geological calibration of spallation production rates in the CRONUS-Earth project. *Quaternary Geochronology* 31, 188–198.

Brisset, E., Guiter, F., Miramont, C., Revel, M., Anthony, E.J., Delhon, C., Arnaud, F., Malet, E., de Beaulieu, J.-L., 2015. Lateglacial/Holocene environmental changes in the Mediterranean Alps inferred from lacustrine sediments. *Quaternary Science Reviews* 110, 49–71.

Buckenham, M.H., Rogers, J., 1954. Flotation of quartz and feldspar by dodecylamine. *Transactions of Institute of Mining and Metallurgy* 64, 1–30.

Casazza, G., Grassi, F., Zecca, G., Minuto, L., 2016. Phylogeographic Insights into a Peripheral Refugium: The Importance of Cumulative Effect of Glaciation on the Genetic Structure of Two Endemic Plants. *PloS one Public Library of Science* 11, e0166983.

Cheddadi, R., Yu, G., Guiot, J., Harrison, S.P., Prentice, I.C., 1996. The climate of Europe 6000 years ago. *Climate Dynamics Springer* 13, 1–9.

Claude, A., Ivy-Ochs, S., Kober, F., Antognini, M., Salcher, B., Kubik, P.W., 2014. The Chironico landslide (Valle Leventina, southern Swiss Alps): age and evolution. *Swiss*

Journal of Geosciences 107, 273–291.

Collins, W.D., Bitz, C.M., Blackmon, M.L., Bonan, G.B., Bretherton, C.S., Carton, J.A., Chang, P., Doney, S.C., Hack, J.J., Henderson, T.B., Others, 2006. The community climate system model version 3 (CCSM3). *Journal of Climate* 19, 2122–2143.

Davis, B.A.S., Brewer, S., Stevenson, A.C., Guiot, J., 2003. The temperature of Europe during the Holocene reconstructed from pollen data. *Quaternary Science Reviews* 22, 1701–1716.

Durand, Y., Giraud, G., Laternser, M., Etchevers, P., Mérindol, L., Lesaffre, B., 2009a. Reanalysis of 47 years of climate in the French Alps (1958–2005): climatology and trends for snow cover. *Journal of Applied Meteorology and Climatology* 48, 2487–2512.

Durand, Y., Laternser, M., Giraud, G., Etchevers, P., Lesaffre, B., Mérindol, L., 2009b. Reanalysis of 44 yr of climate in the French Alps (1958–2002): methodology, model validation, climatology, and trends for air temperature and precipitation. *Journal of Applied Meteorology and Climatology* 48, 429–449.

Fechtig, H., Kalbitzer, S., 1966. The diffusion of argon in potassium-bearing solids. *Potassium argon dating*. Springer, pp. 68–107.

Federici, P.R., Granger, D.E., Pappalardo, M., Ribolini, A., Spagnolo, M., Cyr, A.J., 2008. Exposure age dating and Equilibrium Line Altitude reconstruction of an Egesen moraine in the Maritime Alps, Italy. *Boreas* 37, 245–253.

Federici, P.R., Granger, D.E., Ribolini, A., Spagnolo, M., Pappalardo, M., Cyr, A.J., 2012. Last Glacial Maximum and the Gschnitz stadial in the Maritime Alps according to ¹⁰Be cosmogenic dating. *Boreas* 41, 277–291.

- Federici, P.R., Pappalardo, M., Ribolini, A., 2003. Geomorphological map of the Maritime Alps Natural Park and surroundings (Argentera Massif, Italy). 1: 25,000 scale. Selca, Florence.
- Federici, P.R., Ribolini, A., Spagnolo, M., 2017. Glacial history of the Maritime Alps from the Last Glacial Maximum to the Little Ice Age. Geological Society, London, Special Publications 433, 137–159.
- Gandouin, E., Franquet, E., 2002. Late Glacial and Holocene chironomid assemblages in Lac Long Inférieur (southern France, 2090 m): palaeoenvironmental and palaeoclimatic implications. *Journal of Paleolimnology* 28, 317–328.
- Gardner, A.S., Sharp, M.J., Koerner, R.M., Labine, C., Boon, S., Marshall, S.J., Burgess, D.O., Lewis, D., 2009. Near-surface temperature lapse rates over Arctic glaciers and their implications for temperature downscaling. *Journal of Climate* 22, 4281–4298.
- Gourbet, L., Shuster, D.L., Balco, G., Cassata, W.S., Renne, P.R., Rood, D., 2012. Neon diffusion kinetics in olivine, pyroxene and feldspar: retentivity of cosmogenic and nucleogenic neon. *Geochimica et Cosmochimica Acta* 86, 21–36.
- Granger, D.E., Lifton, N.A., Willenbring, J.K., 2013. A cosmic trip: 25 years of cosmogenic nuclides in geology. *Geological Society of America Bulletin* 125, 1379–1402.
- Hall, K., Lindgren, B.S., Jackson, P., 2005. Rock albedo and monitoring of thermal conditions in respect of weathering: some expected and some unexpected results. *Earth Surface Processes and Landforms* 30, 801–812.
- Harrison, S.P., Bartlein, P.J., Izumi, K., Li, G., Annan, J., Hargreaves, J., Braconnot, P., Kageyama, M., 2015. Evaluation of CMIP5 palaeo-simulations to improve climate

projections. *Nature Climate Change* 5, 735–743.

Harrison, T.M., Lovera, O.M., Matthew, T.H., 1991. $^{40}\text{Ar}/^{39}\text{Ar}$ results for alkali feldspars containing diffusion domains with differing activation energy. *Geochimica et Cosmochimica Acta* 55, 1435–1448.

He, F., 2011. Simulating transient climate evolution of the last deglaciation with CCSM 3. PhD, University of Wisconsin-Madison.

Heilbronner, R., Barrett, S., 2013. Image analysis in Earth sciences: microstructures and textures of earth materials. Springer.

Heiri, O., Brooks, S.J., Renssen, H., Bedford, A., Hazekamp, M., Ilyashuk, B., Jeffers, E.S., Lang, B., Kirilova, E., Kuiper, S., Others, 2014. Validation of climate model-inferred regional temperature change for late-glacial Europe. *Nature Communications* 5, 4914.

Heiri, O., Millet, L., 2005. Reconstruction of Late Glacial summer temperatures from chironomid assemblages in Lac Lautrey (Jura, France). *Journal of Quaternary Science* 20, 33–44.

Heiri, O., Tinner, W., Lotter, A.F., 2004. Evidence for cooler European summers during periods of changing meltwater flux to the North Atlantic. *Proceedings of the National Academy of Sciences* 101, 15285–15288.

Heyman, J., Stroeve, A.P., Harbor, J.M., Caffee, M.W., 2011. Too young or too old: Evaluating cosmogenic exposure dating based on an analysis of compiled boulder exposure ages. *Earth and Planetary Science Letters* 302, 71–80.

Hippe, K., Ivy-Ochs, S., Kober, F., Zasadni, J., Wieler, R., Wacker, L., Kubik, P.W., Schlüchter, C., 2014. Chronology of Lateglacial ice flow reorganization and deglaciation in the

Gotthard Pass area, Central Swiss Alps, based on cosmogenic ^{10}Be and in situ ^{14}C .
 Quaternary geochronology 19, 14–26.

Ilyashuk, E.A., Koinig, K.A., Heiri, O., Ilyashuk, B.P., Psenner, R., 2011. Holocene temperature variations at a high-altitude site in the Eastern Alps: a chironomid record from Schwarzsee ob Sölden, Austria. Quaternary Science Reviews 30, 176–191.

Ivy-Ochs, S., Kober, F., Alfimov, V., Kubik, P.W., Synal, H.-A., 2007. Cosmogenic ^{10}Be , ^{21}Ne and ^{36}Cl in sanidine and quartz from Chilean ignimbrites. Nuclear Instruments & Methods in Physics Research B 259, 588–594.

Jost, A., Lunt, D., Kageyama, M., Abe-Ouchi, A., Peyron, O., Valdes, P.J., Ramstein, G., 2005. High-resolution simulations of the last glacial maximum climate over Europe: a solution to discrepancies with continental palaeoclimatic reconstructions?. Climate Dynamics Springer 24, 577–590.

Kessler, M.A., Anderson, R.S., Stock, G.M., 2006. Modeling topographic and climatic control of east-west asymmetry in Sierra Nevada glacier length during the Last Glacial Maximum. Journal of Geophysical Research: Earth Surface 111.

Ketcham, R.A., 2005. Computational methods for quantitative analysis of three-dimensional features in geological specimens. Geosphere 1, 32–41.

Kuhlemann, J., Rohling, E.J., Krumrei, I., Kubik, P., Ivy-Ochs, S., Kucera, M., 2008. Regional synthesis of Mediterranean atmospheric circulation during the Last Glacial Maximum. Science 321, 1338–1340.

Lal, D., 1987. Production of ^3He in terrestrial rocks. Chemical Geology 66, 89–98.

Larocque, I., Finsinger, W., 2008. Late-glacial chironomid-based temperature reconstructions for

Lago Piccolo di Avigliana in the southwestern Alps (Italy). *Palaeogeography, Palaeoclimatology, Palaeoecology* 257, 207–223.

Liu, Z., Otto-Bliesner, B.L., He, F., Brady, E.C., Tomas, R., Clark, P.U., Carlson, A.E., Lynch-Stieglitz, J., Curry, W., Brook, E., Others, 2009. Transient simulation of last deglaciation with a new mechanism for Bølling-Allerød warming. *Science* 325, 310–314.

Loomis, S.E., Russell, J.M., Verschuren, D., Morrill, C., De Cort, G., Damsté, J.S.S., Olago, D., Eggermont, H., Street-Perrott, F.A., Kelly, M.A., 2017. The tropical lapse rate steepened during the Last Glacial Maximum. *Science Advances* 3, e1600815.

Lovera, O.M., Grove, M., Mark Harrison, T., Mahon, K.I., 1997/8. Systematic analysis of K-feldspar $^{40}\text{Ar}/^{39}\text{Ar}$ step heating results: I. Significance of activation energy determinations. *Geochimica et Cosmochimica Acta* 61, 3171–3192.

Lovera, O.M., Richter, F.M., 1989. The $^{40}\text{Ar}/^{39}\text{Ar}$ Thermochronometry for Slowly Cooled Samples. *Journal of Geophysical Research* 94, 17–917.

Lovera, O.M., Richter, F.M., Harrison, T.M., 1991. Diffusion domains determined by ^{39}Ar released during step heating. *Journal of Geophysical Research* 96, 2057–2069.

Luetscher, M., Boch, R., Sodemann, H., Spötl, C., Cheng, H., Edwards, R.L., Frisia, S., Hof, F., Müller, W., 2015. North Atlantic storm track changes during the Last Glacial Maximum recorded by Alpine speleothems. *Nature Communications* 6, 6344.

Masson-Delmotte, V., Schulz, M., Abe-Ouchi, A., Beer, J., Ganopolski, A., González Rouco, J.F., Jansen, E., Lambeck, K., Luterbacher, J., Naish, T., Osborn, T., Otto-Bliesner, B., Quinn, T., Ramesh, R., Rojas, M., Shao, X., Timmermann, A., 2013. Information from paleoclimate archives. In: Stocker, T.F., Qin, D., Plattner, G.-K., Tignor, M., Allen, S.K.,

- Boschung, J., Nauels, A., Xia, Y., Bex, V., Midgley, P.M. (Eds.), Climate Change 2013: The Physical Science Basis. Contribution of Working Group I to the Fifth Assessment Report of the Intergovernmental Panel on Climate Change. Cambridge University Press, pp. 383–464.
- McGreevy, J.P., 1985. Thermal properties as controls on rock surface temperature maxima, and possible implications for rock weathering. *Earth Surface Processes and Landforms* 10, 125–136.
- Monegato, G., Scardia, G., Hajdas, I., Rizzini, F., Piccin, A., 2017. The Alpine LGM in the boreal ice-sheets game. *Scientific Reports* 7, 2078.
- Nishiizumi, K., Imamura, M., Caffee, M.W., Southon, J.R., Finkel, R.C., McAninch, J., 2007. Absolute calibration of ^{10}Be AMS standards. *Nuclear Instruments & Methods in Physics Research B* 258, 403–413.
- Putkonen, J., Swanson, T., 2003. Accuracy of cosmogenic ages for moraines. *Quaternary Research* 59, 255–261.
- Schmidt, G.A., Annan, J.D., Bartlein, P.J., Cook, B.I., Guilyardi, E., Hargreaves, J.C., Harrison, S.P., Kageyama, M., LeGrande, A.N., Konecky, B., Lovejoy, S., Mann, M.E., Masson-Delmotte, V., Risi, C., Thompson, D., Timmermann, A., Tremblay, L.-B., Yiou, P., 2014. Using palaeo-climate comparisons to constrain future projections in CMIP5. *Climate of the Past* 10, 221–250.
- Schmittner, A., Urban, N.M., Shakun, J.D., Mahowald, N.M., Clark, P.U., Bartlein, P.J., Mix, A.C., Rosell-Melé, A., 2011. Climate sensitivity estimated from temperature reconstructions of the Last Glacial Maximum. *Science* 334, 1385–1388.

924 Schneider, C.A., Rasband, W.S., Eliceiri, K.W., 2012. NIH Image to ImageJ: 25 years of image
 925 analysis. *Nature Methods* 9, 671–675.

926 Schwarz, N., Schlink, U., Franck, U., Großmann, K., 2012. Relationship of land surface and air
 927 temperatures and its implications for quantifying urban heat island indicators--An
 928 application for the city of Leipzig (Germany). *Ecological indicators* 18, 693–704.

929 Shuster, D.L., Cassata, W.S., 2015. Paleotemperatures at the lunar surfaces from open system
 930 behavior of cosmogenic ^{38}Ar and radiogenic ^{40}Ar . *Geochimica et Cosmochimica Acta*
 931 155, 154–171.

932 Shuster, D.L., Farley, K.A., 2005. Diffusion kinetics of proton-induced ^{21}Ne , ^3He , and ^4He in
 933 quartz. *Geochimica et Cosmochimica Acta* 69, 2349–2359.

934 Shuster, D.L., Farley, K.A., Sisterson, J.M., Burnett, D.S., 2004. Quantifying the diffusion
 935 kinetics and spatial distributions of radiogenic ^4He in minerals containing proton-induced
 936 ^3He . *Earth and Planetary Science Letters* 217, 19–32.

937 Stone, J.O., 2000. Air pressure and cosmogenic isotope production. *Journal of Geophysical*
 938 *Research: Solid Earth* 105, 23753–23759.

939 Tremblay, M.M., Shuster, D.L., Balco, G., 2014a. Cosmogenic noble gas paleothermometry.
 940 *Earth and Planetary Science Letters* 400, 195–205.

941 Tremblay, M.M., Shuster, D.L., Balco, G., 2014b. Diffusion kinetics of ^3He and ^{21}Ne in quartz
 942 and implications for cosmogenic noble gas paleothermometry. *Geochimica et*
 943 *Cosmochimica Acta* 142, 186–204.

944 Tremblay, M.M., Shuster, D.L., Balco, G., Cassata, W.S., 2017. Neon diffusion kinetics and
 945 implications for cosmogenic neon paleothermometry in feldspars. *Geochimica et*

Cosmochimica Acta 205, 14–30.

Vermeesch, P., Baur, H., Heber, V.S., Kober, F., Oberholzer, P., Schaefer, J.M., Schlüchter, C., Strasky, S., Wieler, R., 2009. Cosmogenic ^3He and ^{21}Ne measured in quartz targets after one year of exposure in the Swiss Alps. *Earth and Planetary Science Letters* 284, 417–425.

von der Heydt, A.S., Dijkstra, H.A., van de Wal, R.S.W., Caballero, R., Crucifix, M., Foster, G.L., Huber, M., Köhler, P., Rohling, E., Valdes, P.J., Ashwin, P., Bathiany, S., Berends, T., van Bree, L.G.J., Ditlevsen, P., Ghil, M., Haywood, A.M., Katzav, J., Lohmann, G., Lohmann, J., Lucarini, V., Marzocchi, A., Pälike, H., Baroni, I.R., Simon, D., Sluijs, A., Stap, L.B., Tantet, A., Viebahn, J., Ziegler, M., 2016. Lessons on Climate Sensitivity From Past Climate Changes. *Current Climate Change Reports* 2, 148–158.

Wu, H., Guiot, J., Brewer, S., Guo, Z., 2007. Climatic changes in Eurasia and Africa at the last glacial maximum and mid-Holocene: reconstruction from pollen data using inverse vegetation modelling. *Climate Dynamics Springer* 29, 211–229.

968

Sample	Latitude (DD)	Longitude (DD)	Elevation (m)	Sample thickness (cm)	Shielding factor
PDP10	44.421534	7.819950	1806	3	0.9200
PM1	44.252667	7.385500	860	3	0.9653
PM4	44.252667	7.385500	860	3	0.9653
TDB1	44.289712	7.432528	770	3	0.9825
TDB3	44.289712	7.432528	770	3	0.9819

969

970 **Table 1:** Locations and sample information for moraine boulders in the Gesso Valley previously

971 exposure dated with cosmogenic ^{10}Be , originally reported in Federici et al. (2012, 2008).

972

973

974

975

976

977

978

979

980

981

982

983

984

985

986

Sample, aliquot	Mass of quartz analyzed (g)	[³ He] (10 ³ atoms/g)		
PDP10-1	0.109	2.20	±	0.38
PDP10-2	0.101	2.38	±	0.37
PDP10-3	0.102	3.65	±	0.35
PDP10-4	0.126	2.91	±	0.26
PDP10-5	0.121	2.99	±	0.39
PDP10-6	0.136	2.99	±	0.31
PDP10-7	0.117	3.12	±	0.37
PDP10-8	0.125	2.44	±	0.35
PM1-1	0.101	1.14	±	0.42
PM1-2	0.101	0.89	±	0.6
PM1-3	0.304	1.11	±	0.18
PM1-4	0.266	0.88	±	0.15
PM1-5	0.290	1.05	±	0.15
PM4-1	0.113	1.29	±	0.34
PM4-2	0.309	1.51	±	0.17
PM4-3	0.268	1.63	±	0.19
PM4-4	0.247	1.60	±	0.12
TDB1-1	0.216	0.62	±	0.28
TDB1-2	0.269	0.11	±	0.14
TDB1-3	0.306	0.28	±	0.13
TDB1-4	0.292	0.26	±	0.13
TDB1-5	0.482	0.36	±	0.08

TDB3-1	0.216	1.38	±	0.27
TDB3-2	0.124	1.35	±	0.39
TDB3-3	0.279	1.20	±	0.19
TDB3-4	0.301	1.31	±	0.27
TDB3-5	0.268	1.32	±	0.18

Table 2: Observations of cosmogenic ^3He in Gesso Valley quartz samples.

Sample	Apparent exposure age (yr), ^3He			Exposure age (yr), ^{10}Be			^3He retention		
PDP10	6402	±	341	14071	±	1220	0.46	±	0.05
PM1	4534	±	452	16356	±	1601	0.28	±	0.04
PM4	7006	±	512	19213	±	1654	0.36	±	0.04
TDB1	1407	±	271	23397	±	2072	0.06	±	0.01
TDB3	6187	±	561	21003	±	1854	0.29	±	0.04

Table 3: Apparent ^3He exposure ages and retention in Gesso Valley quartz samples. See text for details about the input parameters to the exposure age calculation. Because we have measurements of cosmogenic ^3He from multiple aliquots of each sample, we report weighted mean apparent exposure ages with internal uncertainties alongside weighted mean apparent exposure ages with external uncertainties in parentheses. Because we only have one ^{10}Be measurement per sample, we report a single ^{10}Be exposure age for each sample with internal uncertainty alongside external uncertainty in parentheses. Cosmogenic ^3He retention is calculated using external uncertainties.

Experiment	Domain	E _a (kJ/mol)	ln(D ₀ /a ²)	fraction	Misfit
PDP10-B	1	96.5	10.2	0.61	0.097
	2		16.1	0.21	
	3		13.2	0.18	
PM1-A	1	89.6	8.6	0.54	0.067
	2		10.1	0.36	
	3		14.1	0.1	
PM4-A	1	90.9	8.4	0.74	0.109
	2		5.9	0.2	
	3		14.4	0.06	
TDB1-B	1	99.7	11.8	0.46	0.161
	2		13.2	0.3	
	3		17.3	0.24	
TDB3-B	1	97.6	10.3	0.42	0.149
	2		12.3	0.41	
	3		15.7	0.17	

Table 4: Three domain multiple diffusion domain model parameters for ³He diffusion experiments in Gesso Valley quartz samples.

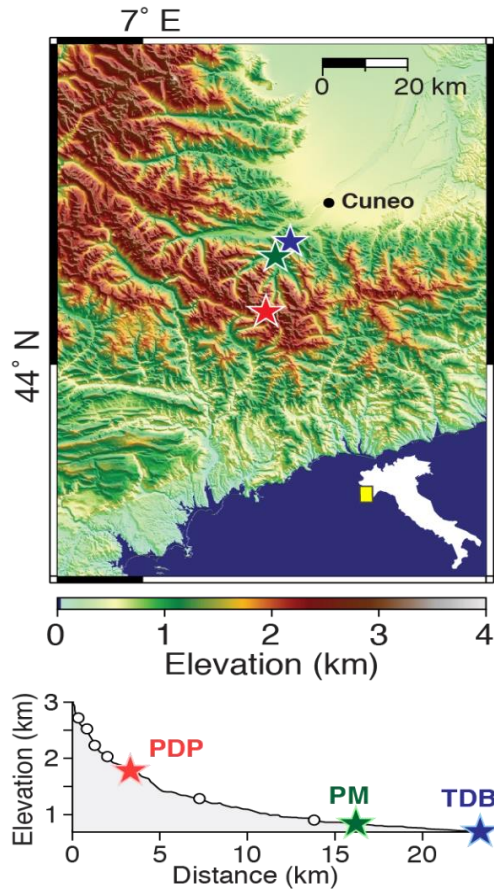


Figure 1: A: Topographic map of the Maritime Alps. Map location is shown in the inset of Italy. White box corresponds to the enlarged view in (B). B: Topography of the Gesso Valley. White stars mark the locations of moraines sampled for this study: Piano del Praiet (PDP), Ponte Murato (PM), and Tetti del Bandito (TDB). Dashed line corresponds to the longitudinal profile shown in (C). C: Longitudinal profile of the Gesso Valley. White stars mark the locations of moraines studied here, as in (B); white circles denote additional moraines in the Gesso Valley not studied here. A detailed map of the geomorphic features in the Gesso Valley is available in Federici et al. (2003). For interpretation of references to color in this figure, refer to the web version of this article.

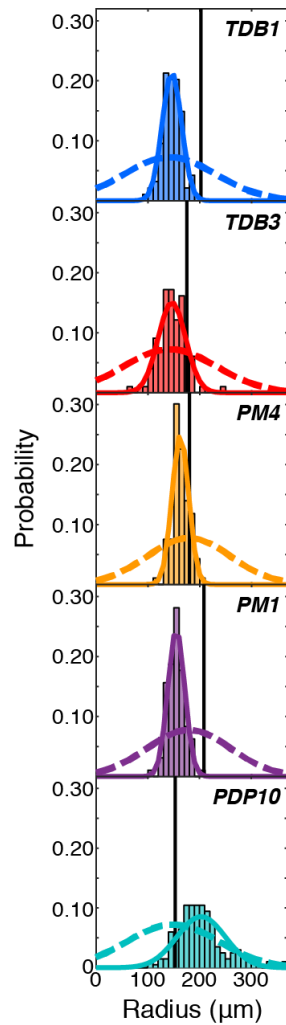


Figure 2: Grain size analysis for Gesso Valley samples. Histograms and solid curves denote the distribution of spherical equivalent radii for representative quartz grains (≥ 100) from the sieve fraction analyzed for cosmogenic ^3He abundances. Dashed curves denote the distribution of spherical equivalent radii in whole rock, inverted from the distribution of sectional circles of quartz grains (≥ 100) measured in thin section. Thin sections were made from the same sample as the crushed fraction, in the case of PDP10, or from a resampled boulder on the same moraine, in all other cases. Vertical black lines denote the spherical equivalent radius of the single quartz grain

analyzed in each diffusion experiment shown in Fig. 4. For interpretation of references to color in this figure, refer to the web version of this article.

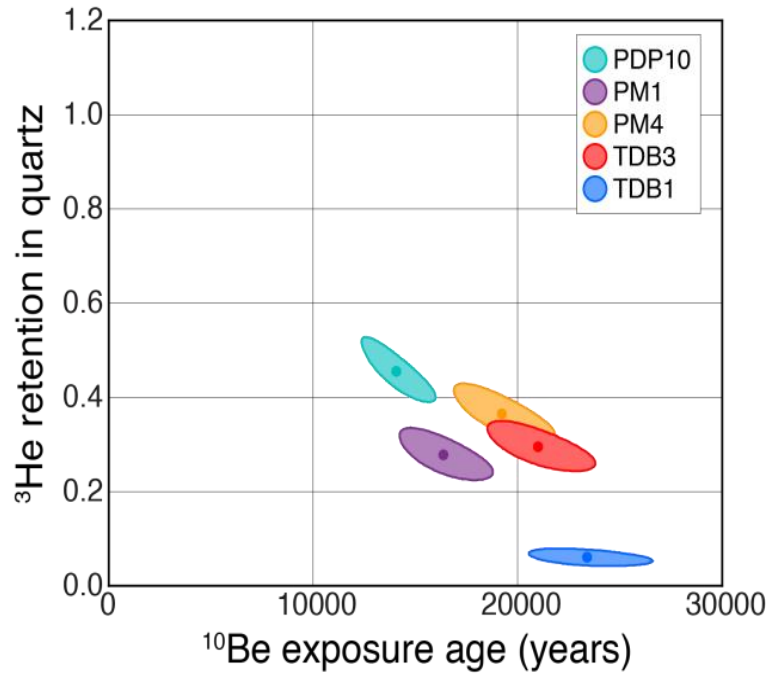


Figure 3: Cosmogenic ^3He retention as a function of ^{10}Be exposure age in quartz from Gesso Valley moraine samples. Ellipses represent 1σ uncertainty. For interpretation of references to color in this figure, refer to the web version of this article.

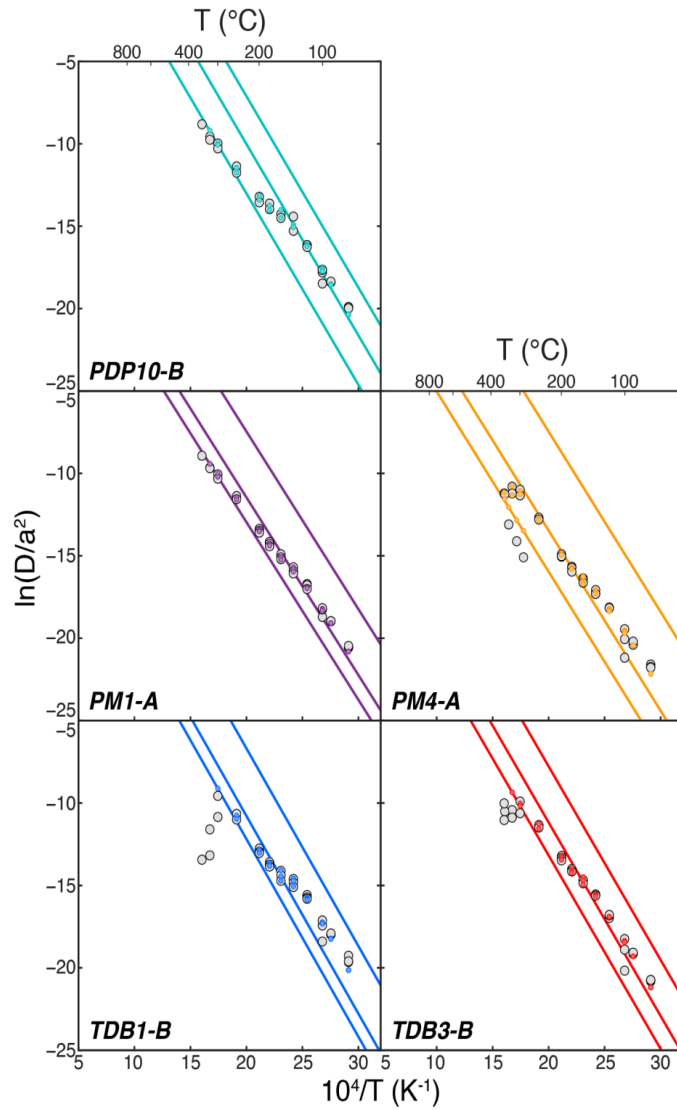


Figure 4: Arrhenius plots for helium diffusion experiments on Gesso Valley quartz samples. D/a^2 values are normalized to s^{-1} . Experimental data are plotted as gray circles. Diffusivities were calculated using the equations of Fechtig and Kalbitzer (1966) and the uncertainty propagation outlined in Tremblay et al. (2014b). Color circles and lines denote three-domain multiple diffusion domain (MDD) models that minimize misfit with the experimental data. Tremblay et al. (2017) describe MDD modeling approach used here. For interpretation of references to color in this figure, refer to the web version of this article.

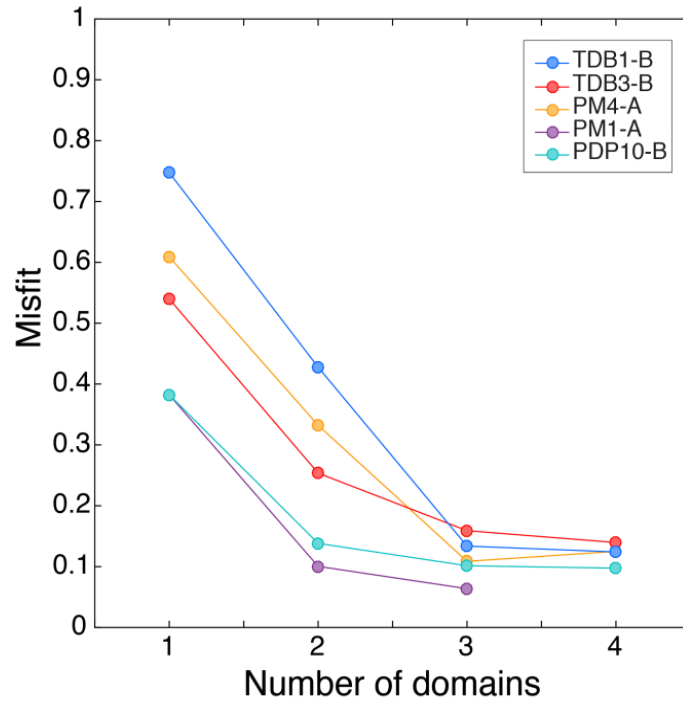


Figure 5: Minimized misfit between observed and MDD-modeled ^3He diffusivities as a function of number of diffusion domains for Gesso Valley quartz samples. We increased the number of diffusion domains in our MDD models until the addition of another diffusion domain did not significantly reduce the misfit between the observed and calculated diffusivities. For all Gesso Valley quartz samples, we found that increasing the number of domains from three to four only marginally improved the misfit; therefore we use three-domain MDD models in subsequent calculations. For experiment PM1-A, attempts at constructing a four domain model yielded two domains with the same pre-exponential factor and thus are the equivalent of the three domain model. For interpretation of references to color in this figure, refer to the web version of this article.

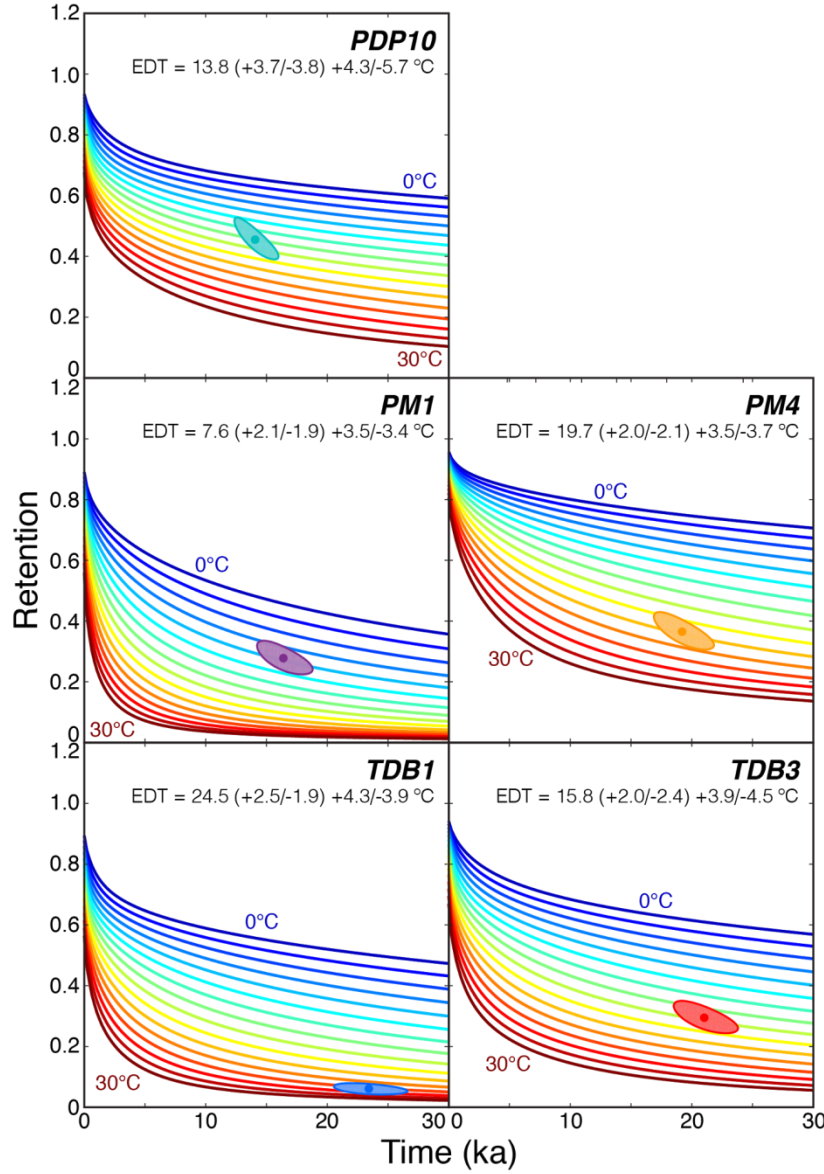


Figure 6: EDTs integrated over the exposure duration of Gesso Valley moraine samples. For each sample, we plot cosmogenic ^3He retention as a function of exposure duration for constant EDTs ranging from 0 to 30 °C in 2 °C increments, and assuming the MDD model diffusion kinetics reported in Table 3. Observed cosmogenic ^3He retention ellipses are plotted as in Fig. 4 for comparison. One set of EDT uncertainties in parentheses accounts for the uncertainty in ^3He retention and exposure duration as determined from ^{10}Be measurements; the second set of

uncertainties accounts for uncertainty in the spherical equivalent radius to which the experimentally-determined diffusion kinetics are scaled in addition to the uncertainties in ^3He retention and exposure duration.

For interpretation of references to color in this figure, refer to the web version of this article.

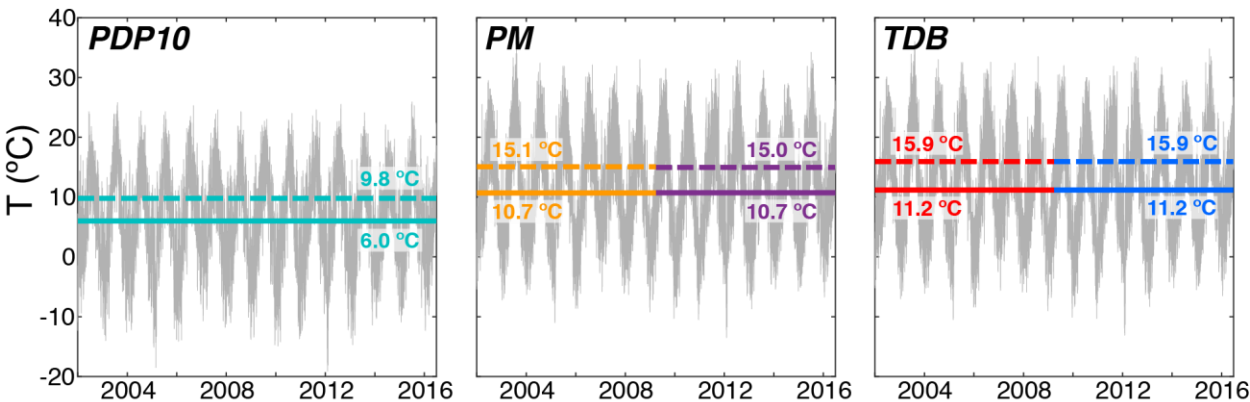


Figure 7: EDTs calculated from modern meteorological data. In gray we show the time series of mean, minimum, and maximum daily temperatures from 2002 to mid-2016 at the elevations of the PDP, PM, and TDB moraines, scaled from the nearest two meteorological stations using average monthly lapse rates. Solid black bars denote the mean temperature for each time series; dashed black bars denote the modern EDT for each time series calculated using the activation energies of the best fit MDD models in Fig. 4 and Table 4. EDTs integrated over the exposure duration of each sample are also shown for comparison as circles, with colors for specific samples and 1σ uncertainties as reported in Fig. 6. For interpretation of references to color in this figure, refer to the web version of this article.

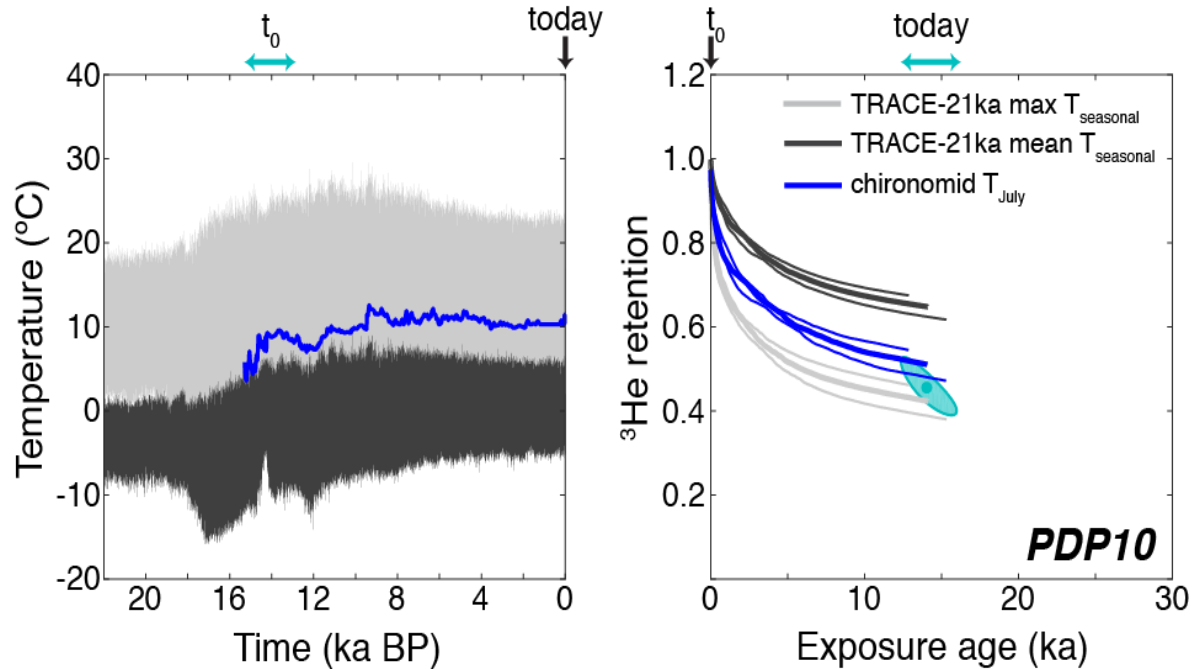


Figure 8: Cosmogenic ^3He retention in PDP10 quartz calculated from scaled TraCE-21ka seasonal temperatures and scaled, spliced chironomid July temperatures. The left panel shows the mean (black) and maximum (gray) seasonal temperature from the TraCE-21ka climate simulation and the mean July temperature (blue) from four spliced chironomid records, scaled to the elevation of PDP10 using modern lapse rate data and, for the chironomid records, weighted by distance from our study site. The right panel shows the evolution of ^3He retention with time assuming the TraCE-21ka and chironomid temperatures represent the EDT experience over PDP10's exposure duration. Thick retention curves assume the mean exposure duration and grain size for diffusion kinetics scaling; lower thin retention curves assume the $+1\sigma$ exposure duration and grain size, while upper thin curves assume the -1σ exposure duration and grain size. The ellipse shows the observed retention and exposure duration, as in Fig. 3. For interpretation of references to color in this figure, refer to the web version of this article.

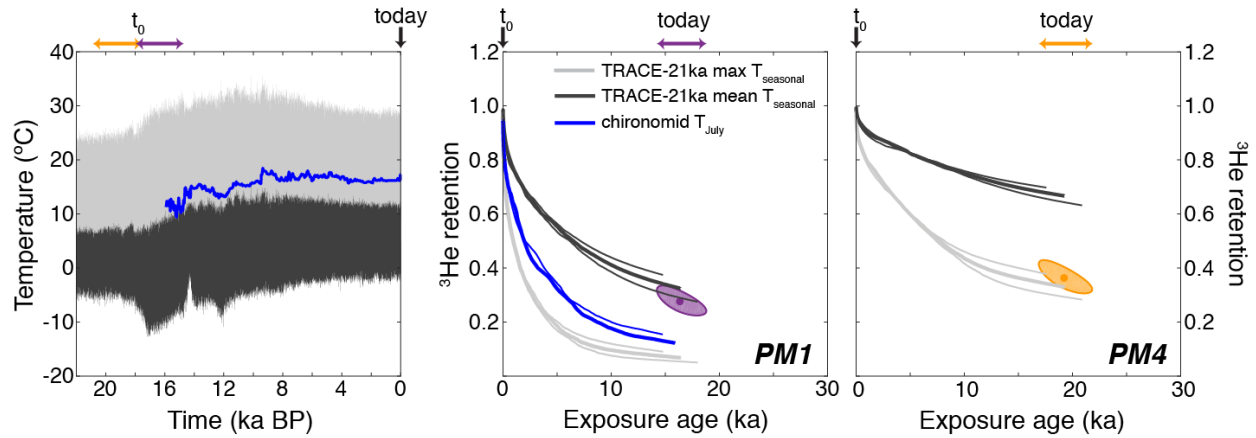


Figure 9: Cosmogenic ^3He retention in PM1 and PM4 calculated from scaled TraCE-21ka seasonal temperatures and, in the case of PM1, scaled, spliced chironomid July temperatures. The left panel shows the mean (black) and maximum (gray) seasonal temperature from the TraCE-21ka climate simulation and the mean July temperature (blue) from four spliced chironomid records, scaled to the elevation of PM using modern lapse rate data and, for the chironomid records, weighted by distance from our study site. The right panels show the evolution of ^3He retention with time assuming the TraCE-21ka and chironomid temperatures represent the EDT experience over the PM samples' exposure duration. Thick and thin retention curves are as in Fig. 8. Ellipses show the observed retention and exposure duration, as in Fig. 3. For interpretation of references to color in this figure, refer to the web version of this article.

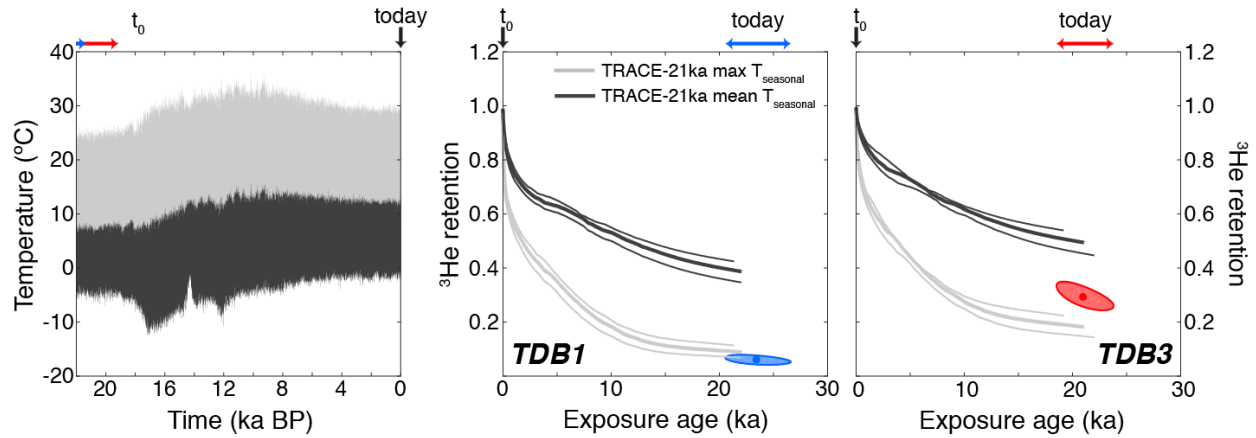


Figure 10: Cosmogenic ^3He retention calculated in TDB1 and TDB3 from scaled TraCE-21ka seasonal temperatures. The left panel shows the mean and maximum seasonal temperature from the TraCE-21ka climate simulation, scaled to the elevation of the TDB moraine using modern lapse rate data. The right panels show the evolution of ^3He retention with time assuming the TraCE-21ka temperatures represent the EDT experience over the TDB samples' exposure duration. Thick and thin retention curves are as in Fig. 8. Ellipses show the observed retention and exposure duration, as in Fig. 3. For interpretation of references to color in this figure, refer to the web version of this article.

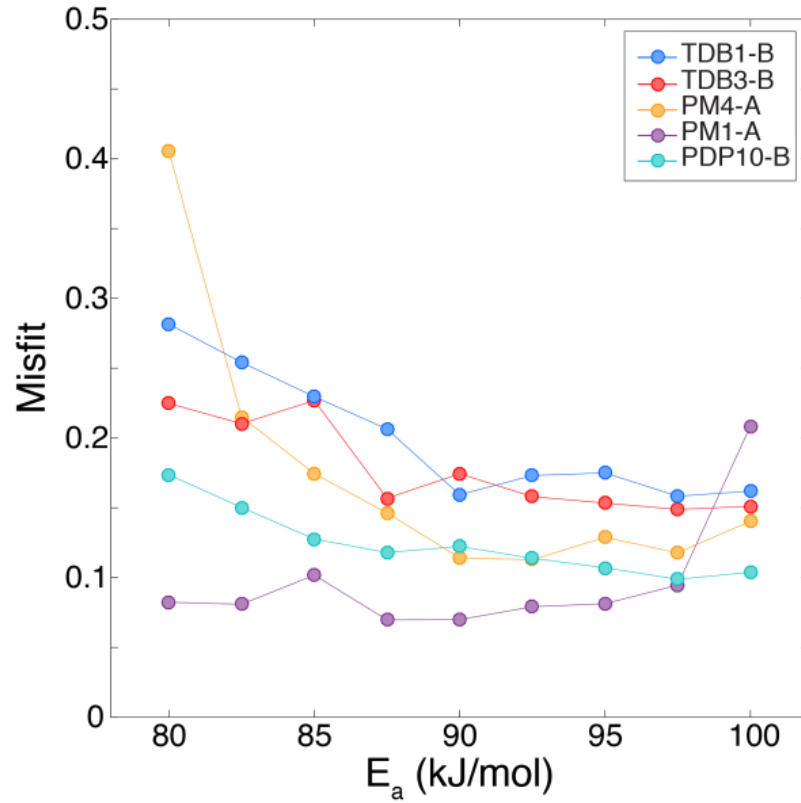


Figure 11: Minimized misfit between observed and MDD-modeled ^3He diffusivities as a function of activation energy E_a for Gesso Valley quartz samples, assuming a three domain diffusion model. Pre-exponential factors and gas fractions for each domain covary with E_a ; we show misfit as a function of E_a because it is assumed to be common to all diffusion domains in our modeling approach. For interpretation of references to color in this figure, refer to the web version of this article.